Masterthesis

Parameter space explorations of scotogentic models using artificial intelligence

Andreas Karle

Würzburg, January 15, 2024

Julius-Maximilians-Universität Würzburg
Department of Theoretical Physics II
Supervisor: Prof. Dr. Werner Porod

Abstract

The Standard Model (SM) falls short in explaining phenomena such as neutrino masses, the anomalous magnetic moment of the muon and dark matter. This makes the need of physics beyond the Standard Model (BSM) evident. Scotogenic Models are a collection of BSM theories, which introduce a $\mathbb{Z}_2$ symmetry under which SM particles are even and new BSM particles are odd. They can generate naturally small neutrino masses and provide a dark matter candidate. This thesis considers the T1-2-A' variant of Scotogenic models, which was proposed in the work of Alvarez et al. [1] and can additionally explain the anomalous magnetic moment of the muon.
Central to this work is the test of novel techniques to search the parameter space of the T1-2-A' model. Therefore the evolutionary algorithms NSGA-III and CMA-ES are introduced and utilized to find valid parameter sets, given constraints from neutrino data, the anomalous magnetic moment of the muon, charged lepton flavour violating (CLFV) processes and the dark matter (DM) relic density. NSGA-III is a multiobjective optimization algorithm, while CMA-ES is designed for single objective optimization. A modification of the CMA-ES algorithm (h-CMA-ES) is proposed, which introduces a hierarchy to the objectives and greatly improves the convergence rate. Additionally the results are compared to a previous MCMC scan [1] of the T1-2-A' model, where a modified Casas-Ibarra parametrization of the Yukawa like couplings was utilized, to ensure a proper fit of neutrino data and the anomalous magnetic moment of the muon. This comparison is done for the Yukawa like couplings, processes involving CLFV and DM candidates.
The h-CMA-ES algorithm yields parameter sets that exhibit a more comprehensive coverage of the parameter space compared to NSGA-III, which tends to generate parameter sets in a smaller sub region. Notably h-CMA-ES provides a 46% higher sampling efficiency when compared to NSGA-III. Both NSGA-III and h-CMA-ES demonstrate the capability to reproduce parts of the parameter regions found by the previous MCMC scan, and additionally provide parameter sets outside the scope of the MCMC scan.
Lastly, a brief analysis of LHC phenomenology is conducted.

Zusammenfassung

Das Standardmodell (SM) scheitert dabei, Phänomene wie Neutrino-Massen, das anomale magnetische Moment des Myons und Dunkle Materie zu erklären. Dies verdeutlicht die Notwendigkeit von Physik jenseits des Standardmodells (BSM).
Scotogenic-Modelle sind eine Sammlung von BSM-Theorien, die eine $\mathbb{Z}_2$-Symmetrie einführen, unter der SM-Teilchen gerade und neue BSM-Teilchen ungerade sind. Sie können auf natürliche Weise geringe Neutrino-Massen erzeugen und liefern einen Dunkle Materie Kandidaten. Diese Arbeit betrachtet die T1-2-A'-Variante der Scotogenic-Modelle, die in der Arbeit von Alvarez et al. [1] entwickelt wurde und zusätzlich das anomale magnetische Moment des Myons erklären kann.
Hauptbestandteil dieser Arbeit ist der Test neuartiger Techniken zur Untersuchung des Parameterraums des T1-2-A' Modells. Dafür werden die evolutionären Algorithmen NSGA-III und CMA-ES eingeführt und verwendet, um gültige Parametersätze zu finden. Dabei werden Einschränkungen durch Neutrino-Daten, dem anomalen magnetische Moment des Myons, Prozesse mit Flavourverletzung der geladenen Leptonen (CLFV) und der Überrest-dichte der Dunklen Materie (DM) berücksichtigt. NSGA-III ist ein Multikriterieller-Optimierungsalgorithmus, während CMA-ES für die Optimierung nach einem einzigen Ziel entworfen wurde. Es wird eine Modifikation des CMA-ES-Algorithmus (h-CMA-ES) vorgeschlagen, die eine Hierarchie in die Ziele einführt und die Konvergenzrate erheblich verbessert.
Zusätzlich werden die Ergebnisse mit einem früheren MCMC-Scan [1] des T1-2-A'-Modells verglichen, bei dem eine modifizierte Casas-Ibarra-Parametrisierung der Yukawa-ähnlichen Kopplungen verwendet wurde, um eine Anpassung der Neutrino-Daten und dem anomalen magnetischen Moment des Myons zu gewährleisten. Dieser Vergleich erfolgt für die Yukawa-ähnlichen Kopplungen, Prozesse mit CLFV und dem DM-Kandidaten.
Der h-CMA-ES-Algorithmus liefert Parametersätze, die im Vergleich zu NSGA-III eine umfassendere Abdeckung des Parameterraums aufweisen. h-CMA-ES zeigt insbesondere eine 46% höhere Stichprobeneffizienz im Vergleich zu NSGA-III. Sowohl NSGA-III als auch h-CMA-ES zeigen die Fähigkeit, Teile des Parameterraums zu reproduzieren, die durch den vorherigen MCMC-Scan gefunden wurden, und liefern zusätzlich Parametersätze außerhalb des Parameterbereichs des MCMC-Scans.
Abschließend wird eine kurze Analyse der LHC-Phänomenologie durchgeführt.

Contents

Chapter 1

Introduction

The Standard Model of Particle Phyics (SM) stands as the pinnacle of achievements in the realm of particle physics, providing a remarkably accurate and comprehensive framework for elementary particles and their interactions. Measurements from Tevatron [2] at Fermilab, the Large Electron–Positron Collider (LEP) [3] and the Large Hadron Collider (LHC) [4] in CERN have validated its predictions to great accuracy.
Despite its successes, the Standard Model is not without its puzzles. In the SM neutrinos are considered massless, but through observations of solar neutrinos and further experiments [5, 6], the process of neutrino flavour oscillations became evident. This can only be explained by attributing a non zero mass to neutrinos. With the mechanism behind neutrino mass generation remaining an open question up until today, the need to extend the SM is evident.
Another intriguing anomaly lies in the anomalous magnetic moment of the muon, as measured at Fermilab in 2021 [7]. The experimental result deviates from the Standard Model prediction by 4.2σ and latest results show an even greater deviation [8]. This suggests the existence of unknown particles or forces that may be influencing the magnetic properties of the muon.
Additional problems arise from observations of galaxy rotation curves and cosmic microwave background radiation. They strongly support the existence of dark matter [9, 10], a type of matter that only interacts gravitationally and maybe through the weak force and an additional symmetry. In the ΛCDM model of cosmology dark matter makes up 85% of all matter in the universe [11]. This phenomenon can only be explained by a new theory of gravity or new particles, as the SM can not provide a suitable candidate.
While the SM has proven remarkably successful in describing particle physics phenomena within certain energy regimes, its inability to address neutrino masses, the muon's anomalous magnetic moment, and the nature of dark matter signals the need for new theoretical frameworks.
The most common method to resolve these issues is to introduce new physics beyond the

Standard model (BSM). There are many BSM models using different techniques to explain the inconsistencies. This thesis studies one type of these models, called Scotogenic model (from greek: scótos "darkness" + genés "offspring" → "created from darkness"). Scotogenic models introduce a $\mathbb{Z}_2$ symmetry with new BSM particles odd under this symmetry. They produce naturally small Majorana masses on one-loop level for neutrinos and the new symmetry provides a bosonic or fermionic stable dark matter candidate.

The initial Scotogenic model was introduced by Ernest Ma in 2006 [12]. Since then, numerous variations have been put forth to explain both neutrino masses and dark matter in a coherent manner.

In this work the variant denoted as T1-2-A' is discussed. The nomenclature T1-2-A' was developed in [1], where it is derived from the classification system by Restrepo et al. [13]. It serves as an expansion of the original T1-2-A model, addressing its lack of capacity to simultaneously account for the anomalous magnetic moment of the muon, processes involving Charged Lepton Flavor Violation (CLFV), and neutrino masses. The model introduces two new scalar particles, one $SU(2)_L$ singlet, one douplet and four fermions, split into 2 singlets and two Weyl fermion doublets. These new particles are odd under the new $\mathbb{Z}_2$, while SM particles remain even. This model is able to radiatively generate neutrino masses, can explain the anomalous magnetic moment of the muon and has a stable dark matter candidate.

This work is dedicated to explore the parameter space of the T1-2-A' model using novel techniques. Therefore the evolutionary algorithms NSGA-III [14] and CMA-ES [15] are introduced and utilized to search the parameter space. An additional aspect involves comparing the results to a previous search for this model using Markov Chain Monte Carlo (MCMC) methods by Alvarez et al. [1]. And investigate the differences derived from the different methods. In their search they modified the Casas-Ibarra (CI) parametrization [16] to reduce the complexity of the parameter space of the T1-2-A' model, whilst simultaneously also reducing the parameter space. On the contrary, no such simplifications were made for the parameter search in this work. The aim is to see if these novel methods yield parameter sets despite the higher complexity and if there are viable regions of the parameter space outside the ones previously found.

This thesis is structured as follows. The 2. chapter introduces fundamental topics and presents the relevant measurements for the later parameter search. These include the neutrino mass, the anomalous magnetic moment of the muon, charged lepton flavour violating processes and dark matter.

In chapter 3, the T1-2-A' model is introduced with its new scalar and fermion sector. Additionaly a short outline is given about the generation of neutrino masses at one loop level, the anomalous magnetic moment and the charged lepton flavour violating processes.

Chapter 4 introduces the algorithms NSGA-III and CMA-ES. Therefore a brief introduc-

tion to evolutionary algorithms and multiobjective optimization is provided. Furthermore the adaptation of these algorithms for the T1-2-A' model is described.
In Chapter 5, the results of the parameter search with the evolutionary algorithms are discussed and juxtaposed to the previous MCMC scan. Furthermore, a brief analysis of LHC phenomenology is conducted.

Chapter 2

Physical fundamentals

In this chapter, a selection of physical concepts such as neutrino oscillations and the anomalous magnetic moment of the muon are introduced. Furthermore charged lepton flavour violating processes and Dark Matter will be discussed.

2.1 Neutrino masses

The neutrino, a fundamental particle in the SM, was first postulated by Wolfgang Pauli in 1930 [17] to explain the apparent violation of energy conservation in radioactive beta decay. It took until 1956 that Frederick Reines and Clyde Cowan successfully detected neutrinos emitted from a nuclear reactor and confirming their existence [18].

As the name suggests neutrinos are fermions that possess no electric charge, and consequently, they only interact through the weak force. Neutrinos, beeing a type of lepton, manifest in three distinct flavours: the electron neutrino, muon neutrino and tau neutrino. Due to their exclusively left-handed occurrence, neutrinos lack a Yukawa coupling that would provide them a mass, which explains their apparent masslessness in the Standard Model. The Homestake experiment in the late 1960s, aimed to detect electron neutrinos generated in the sun, found a discrepancy in the flux of expected and measured neutrinos. This gave rise to the solar neutrino problem [5]. Through later experiments, like Super Kamiokande [6], it has become evident that neutrinos can oscillate between flavors, which explains the neutrino flux deficit from the sun. This phenomenon can only be explained by attributing a non-zero mass to neutrinos, suggesting the need for an extension of the Standard Model.

The following derivation of neutrino oscillations is based on [19]. These oscillations are induced by neutrino mixing, which means that neutrino flavour fields are not identical with the neutrino mass eigenfields, but are related through a matrix U which describes the strength of the overlap. Therefore the neutrino flavour states $|\nu_\alpha\rangle$ are linear combinations

of neutrino mass states $|m_j\rangle$:

$$|\nu_\alpha\rangle \;=\; \sum_{i=0}^{3} U^*_{\alpha j}\,|m_j\rangle \;, \tag{2.1}$$

where $|\nu_\alpha\rangle$ is a neutrino with flavour α. This flavour is determined by the charged lepton in the production or detection process.
Since mass eigenstates propagate as plane waves, the propagation state of a neutrino with energy E can be expressed as

$$|\nu_\alpha, x\rangle \;=\; \sum_{j=1}^{3} U^*_{\alpha j} e^{-i(E_j t - \boldsymbol{p}_j \boldsymbol{x})}\,|m_j\rangle \;, \tag{2.2}$$

with neutrino momenta in the limit of high energies compared to the small neutrino mass

$$p_j \;=\; \sqrt{E^2 - m_j^2} \;\simeq\; E - \frac{m_j^2}{2E} \quad \text{for} \quad E \gg m_j \,. \tag{2.3}$$

Therefore, the probability for a neutrino $|\nu_\alpha, x\rangle$ with flavour α at $x = 0$ to be measured with flavour β at $x = L$ is computed as $|\langle\nu_\beta|\nu_\alpha, L|\nu_\beta|\nu_\alpha, L\rangle|^2$. With the explicit form (2.2) and momentum (2.3), the neutrino transition probability is given by

$$P_{\nu_\alpha \to \nu_\beta}(L/E) \;=\; \left| \sum_{j=1}^{3} U_{\beta j} U^*_{\alpha j} e^{-i m_j^2 L/2E} \right|^2 \,. \tag{2.4}$$

From this equation one can conclude that the transition probability depends only on mass squared differences e.g. $m_2^2 - m_1^2$.
In this basis, the matrix U matches the Pontecorvo-Maki-Nakagawa-Sakata matrix (PMNS-matrix), which can be parameterized with the three mixing angles θ_{12}, θ_{13}, θ_{23} and the charge parity phase δ

$$U_{\text{PMNS}} \;=\; \begin{pmatrix} 1 & 0 & 0 \\ 0 & c_{23} & s_{23} \\ 0 & -s_{23} & c_{23} \end{pmatrix} \begin{pmatrix} c_{13} & 0 & s_{13} e^{-i\delta} \\ 0 & 1 & 0 \\ -s_{13} e^{i\delta} & 0 & c_{13} \end{pmatrix} \begin{pmatrix} c_{12} & s_{12} & 0 \\ -s_{12} & c_{12} & 0 \\ 0 & 0 & 1 \end{pmatrix} \,, \tag{2.5}$$

where $s_{jk} = \sin\theta_{jk}$ and $c_{jk} = \cos\theta_{jk}$. The current best estimates for the values of the mixing angles and the charge-parity phase are [20]

$$\sin^2(\theta_{12}) \;=\; 0.304 \pm 0.012 \,, \tag{2.6}$$

$$\sin^2(\theta_{13}) \;=\; 0.02219^{+0.00062}_{-0.00063} \;=\; \left(22.19^{+0.62}_{-0.63}\right) \cdot 10^{-3} \,, \tag{2.7}$$

$$\sin^2(\theta_{23}) \;=\; 0.573^{+0.016}_{-0.020} \,, \tag{2.8}$$

$$\delta \;=\; 197^{+27}_{-24}\,^\circ \,. \tag{2.9}$$

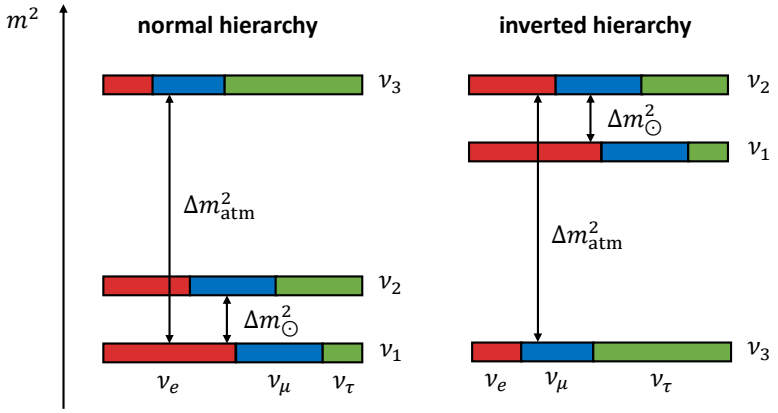

Figure 2.1: The normal and the inverted 3-neutrino mass spectrum.

Due to the extremely small mass of neutrinos, direct measurement is a challenging task. Experiments like KATRIN, employing tritium beta decay, can only provide upper limits ($m_{\nu_{\bar{e}}} < 0.8$ eV/c^2 [21]) for the neutrino mass. As a consequence, more precise information is obtained through neutrino oscillations, but these are limited to mass squared differences. Due to this limitation, the specific ordering of the masses remains unclear, giving rise to the neutrino hierarchy problem. For simplicity, one can assume $m_1 < m_2$, establishing the solar parameter $\Delta m^2_{\odot} = \Delta m^2_{21} = m_2^2 - m_1^2 > 0$ as positive. Consequently, the sign of Δm^2_{31} is undetermined, resulting in two types of mass spectra illustrated in Fig. 2.1. Normal ordering implies $m_3 \gg m_2 > m_1$, while inverted ordering implies $m_3 \ll m_1 < m_2$. The determination of the atmospheric parameter is based on measurements of atmospheric neutrinos and lacks a unique definition. However, a widely adopted convention assumes that Δm^2_{atm} represents the largest possible mass-squared difference. Adhering to this convention, normal ordering corresponds to $\Delta m^2_{\text{atm}} = \Delta m^2_{31}$, and inverted ordering corresponds to $\Delta m^2_{\text{atm}} = \Delta m^2_{23}$.

Due to the current preference for normal ordering over inverted ordering, the following squared mass difference parameters are considered under normal ordering [20]

$$\begin{aligned} \Delta m^2_{\odot} &= \Delta m^2_{21} = 7.42^{+0.21}_{-0.20} \cdot 10^{-23}\,(\text{GeV})^2\,, \\ \Delta m^2_{\text{atm}} &= \Delta m^2_{31} = 2.517^{+0.026}_{-0.028} \cdot 10^{-21}\,(\text{GeV})^2\,. \end{aligned} \tag{2.10}$$

To generate neutrino masses beyond the standard model, new methods must be devised which also should naturally yield small neutrino masses. The T1-2-A' Scotogenic model generates neutrino masses radiatively through one loop diagrams. This approach has the advantage that the mass terms are inherently suppressed by a high energy scale $\propto v^2/\Lambda_0$.

2.2 Muon anomalous magnetic moment

Due to Quantum Electrodynamics (QED), every particle with a non-zero spin possesses a magnetic moment

$$\vec{m} \;=\; g\frac{q}{2m}\vec{S}\,, \tag{2.11}$$

where q represents the charge of the particle, m denotes its mass, $\vec{S}$ signifies the particle's spin, and g represents the gyromagnetic factor or g-factor. For particles with a spin of $\frac{1}{2}$, elementary charge e and mass m_e, the g-factor at the tree level is precisely $g = 2$. This outcome stems directly from the Dirac equation. However, when taking into account higher-order loop corrections, this is no longer true, leading to minor deviations.
To characterize this deviation the anomalous magnetic moment is defined as follows:

$$a_\alpha \;=\; \frac{g_\alpha - 2}{2} \tag{2.12}$$

where $\alpha = \{e, \mu, \tau\}$. The anomalous magnetic moment of the electron is one of the most precisely masuered quantities in the realm of physics. The best experimental value, determined from high precision cyclotron measurements [22], is

$$a_e^{\text{ex}} \;=\; (1\ 159\ 652\ 180\ 59 \pm 13) \cdot 10^{-14}\,. \tag{2.13}$$

This result aligns with the currently best theoretical prediction of [23],

$$a_e^{\text{th}} \;=\; (1\ 159\ 652\ 18 \pm 75) \cdot 10^{-11}\,. \tag{2.14}$$

Such agreement stands as one of the notable achievements of the standard model.
In the case of the muon, discrepancies between experimental measurements and theoretical predictions have persisted for over a decade, suggesting potential new physics beyond the standard model.
In the SM, the anomalous magnetic moment is determined through a perturbative expansion in the fine-structure constant α. This expansion starts with the Schwinger term $\alpha/(2\pi)$ and extends up to and including terms of $\mathcal{O}(\alpha^5)$. Electroweak corrections have been meticulously computed up to the full two-loop order and accounting for dominant three-loop effects. These calculations only introduce minor uncertainties in comparison to experimental uncertainties.
Theoretical uncertainties mainly arise from QCD corrections, particularly hadronic vacuum polarization (HVP) and hadronic light-by-light scattering (Hlbl) [24]. Calculating these effects poses a significant challenge due to their non-perturbative nature. There are two fundamental approaches to calculating these QCD corrections. The data driven approach (DDA) utilizes experimental data from scattering processes. While lattice QCD

discretizes spacetime into distinct points. This makes it possible to make numerical calculations and later take to continuum limit. The problem here arises, because the data driven approaches and lattice QCD give slightly different results for HVP. While lattice calculations tend to agree with the experimental value, the more precise DDA results have a substantial deviation.
As this tension requires further investigation, this work relies on the theoretical value from the white paper [24]:

$$a_\mu^{\text{th}} \;=\; (1\ 165\ 918\ 10 \pm 43) \cdot 10^{-11}\,. \tag{2.15}$$

As for the experimental value, combining FNAL 2021 results [7] with previous BNL 2006 measurements yields an experimental average of:

$$a_\mu^{\text{ex}} \;=\; (1\ 165\ 920\ 61 \pm 41) \cdot 10^{-11}\,. \tag{2.16}$$

This results in a total discrepancy of

$$\Delta a_\mu \;=\; (2.51 \pm 0.59) \cdot 10^{-9}\,, \tag{2.17}$$

equivalent to a deviation of approximately 4.2σ between theory and experiment. Consequently, the anomalous magnetic moment of the muon emerges as an intriguing testing ground for BSM physics.
The latest results from FNAL in October 2023 [8] improved the experimental uncertainties by a factor of 2

$$\begin{aligned} a_\mu^{\text{ex}} \;&=\; (1\ 165\ 920\ 59 \pm 22) \cdot 10^{-11}\,, \\ \Delta a_\mu \;&=\; (2.49 \pm 0.48) \cdot 10^{-9}\,. \end{aligned} \tag{2.18}$$

Which leads to an even greater deviation of about 5.1σ, intensifying the interest in further investigation. However, in this study, the 2021 results are employed due to the comparison with the previous MCMC scan [1]. Moreover these results where published after the data collection for this project began.

2.3 Charged lepton flavour violating processes

Charged lepton flavor violating processes are rare particle interactions in which a charged lepton (e.g., electron, muon, or tau) transforms its flavor, converting into another charged lepton of a different flavour. This transformation typically involves the emission of a photon

$$l_\alpha \to l_\beta \gamma \quad \text{with} \quad \alpha \in \{\mu, \tau\}\,,\ \beta \in \{e, \mu\} \quad \text{and} \quad \alpha \neq \beta\,. \tag{2.19}$$

Additionally there are processes including four leptons:

$$l_\alpha \to l_\beta l_\xi l_\kappa \quad \text{with} \quad \alpha \in \{\mu, \tau\}\,,\ \beta, \xi, \kappa \in \{e, \mu\} \quad \text{and} \quad \alpha \neq \beta, \xi, \kappa\,, \tag{2.20}$$

These CLFV processes have never been observed. However, their existence is somewhat expected, since flavor is not a fundamental symmetry of the SM. Therefore they serve as important precision observables. Additionally, flavour is violated by weak decays of quarks in the CKM matrix and by neutral leptons through neutrino oscillations, as described in section 2.1.
The branching ratios for these processes are calculated from the partial $\Gamma(l_\alpha \to l_\beta \gamma)$ and total $\Gamma_{\text{tot}}(\mu)$ decay width

$$\begin{aligned} \text{BR}[l_\alpha \to l_\beta \gamma] &= \frac{\Gamma(l_\alpha \to l_\beta \gamma)}{\Gamma_{\text{tot}}(l_\alpha)}\,. \\ \text{BR}[l_\alpha \to l_\beta l_\xi l_\kappa] &= \frac{\Gamma(l_\alpha \to l_\beta l_\xi l_\kappa)}{\Gamma_{\text{tot}}(l_\alpha)}\,. \end{aligned} \tag{2.21}$$

As of now, no observations of CLFV processes have been observed, resulting only in upper limits for the branching ratios. Their current best estimate is given by [25]

$$\begin{aligned} \text{BR}[\mu \to e\gamma] &< 4.2 \cdot 10^{-13}\,, & \text{BR}[\tau^- \to \mu^-\mu^+\mu^-] &< 2.1 \cdot 10^{-8}\,, \\ \text{BR}[\tau \to e\gamma] &< 3.3 \cdot 10^{-8}\,, & \text{BR}[\tau^- \to \mu^+ e^- e^-] &< 1.5 \cdot 10^{-8}\,, \\ \text{BR}[\tau \to \mu\gamma] &< 4.2 \cdot 10^{-8}\,, & \text{BR}[\tau^- \to \mu^- e^+ e^-] &< 1.8 \cdot 10^{-8}\,, \\ \text{BR}[\mu^- \to e^- e^+ e^-] &< 1.0 \cdot 10^{-12}\,, & \text{BR}[\tau^- \to \mu^- e^+ \mu^-] &< 1.7 \cdot 10^{-8}\,, \\ \text{BR}[\tau^- \to e^- e^+ e^-] &< 2.7 \cdot 10^{-8}\,, & \text{BR}[\tau^- \to e^- \mu^+ \mu^-] &< 2.7 \cdot 10^{-8}\,. \end{aligned} \tag{2.22}$$

Lepton flavor-violating processes can occur during scattering on the nuclei of elements such as titanium, lead, and gold, leading to strongly constraint conversion ratios

$$\text{CR}_{\mu\to e}(A) = \frac{\Gamma(\mu^- A \to e^- A)}{\Gamma(\mu^- A \to \text{capture})} \quad \text{with} \quad A = \{\text{Ti, Pb, Au}\}\,, \tag{2.23}$$

with the currently best limits [25]

$$\begin{aligned} \text{CR}_{\mu\to e}(Ti) &< 4.3 \cdot 10^{-12}\,, \\ \text{CR}_{\mu\to e}(Pb) &< 4.3 \cdot 10^{-11}\,, \\ \text{CR}_{\mu\to e}(Au) &< 7.0 \cdot 10^{-13}\,. \end{aligned} \tag{2.24}$$

Additionally there are decays for the τ^- to another charged lepton and pion π or a newly introduced scalar η from the Scotogenic model, which have to be considered

$$\begin{aligned} \tau^- &\to l_\alpha \pi \quad \text{with} \quad \alpha = \{\mu, e\}\,, \\ \tau^- &\to l_\alpha \eta \quad \text{with} \quad \alpha = \{\mu, e\}\,. \end{aligned} \tag{2.25}$$

Their current experimental bounds are given by [25]

$$\begin{aligned} \mathrm{BR}[\tau^- \to e^-\pi] &< 8.0 \cdot 10^{-8}\,, & \mathrm{BR}[\tau^- \to \mu^-\pi] &< 1.1 \cdot 10^{-7}\,, \\ \mathrm{BR}[\tau^- \to e^-\eta] &< 9.2 \cdot 10^{-8}\,, & \mathrm{BR}[\tau^- \to \mu^-\eta] &< 6.5 \cdot 10^{-8}\,, \\ \mathrm{BR}[\tau^- \to e^-\eta'] &< 1.6 \cdot 10^{-7}\,, & \mathrm{BR}[\tau^- \to \mu^-\eta'] &< 1.3 \cdot 10^{-7}\,. \end{aligned} \tag{2.26}$$

Lastly the Z^0 boson decay has to be considered, as it can possibly decay into two different charged leptons. This decay is again strongly constraint with the current best limits [25]

$$\begin{aligned} \mathrm{BR}(Z^0 \to e^\pm\mu^\mp) &< 7.5 \cdot 10^{-7}\,, \\ \mathrm{BR}(Z^0 \to e^\pm\tau^\mp) &< 5.0 \cdot 10^{-6}\,, \\ \mathrm{BR}(Z^0 \to \mu^\pm\tau^\mp) &< 6.5 \cdot 10^{-6}\,. \end{aligned} \tag{2.27}$$

2.4 Dark matter

Dark matter is a hypothetical, non-luminous form of matter that constitutes about 85% of the total mass in the universe [11]. Its existence is inferred from its gravitational effects on the visible matter in galaxies and galaxy clusters. The concept of dark matter was first postulated by the Swiss astronomer Fritz Zwicky in 1933 [9] when he observed that the visible matter within the Coma Cluster was insufficient to account for the cluster's gravitational dynamics. Subsequent astrophysical observations, including galaxy rotation curves and the cosmic microwave background radiation, have provided compelling empirical evidence for the existence of dark matter [10].

One theory presumes that dark matter is made up of primordial black holes (PBH), a hypothetical type of black holes that where created in the inflation era of the universe, shortly after the Big Bang [26]. But there are strong constraints on the mass ranges of these PBH [27].

Other theories include axions, a type of particle originally introduced by R. D. Peccei and Helen R. Quinn in 1977 [28], to resolve the strong CP problem [29]. If axions exist within a certain mass range, they are a probable candidate for dark matter.

However, this work looks at the concept of weakly interacting massive particles (WIMPs) as a potential explanation for dark matter [10]. As the name implies, WIMPs solely engage in gravitational interactions and interactions through the weak force. However, no particle fitting this description has been detected thus far. Additionally, introducing a charge under a new symmetry, guarantees a stable dark matter candidate as the lightest particle after electroweak symmetry breaking.

WIMPs are theorized as relic particles from the early Universe when particles were in thermal equilibrium. At high temperatures, dark matter particles and their antiparticles would form and annihilate into lighter particles. As the Universe expanded and cooled,

the thermal energy of these lighter particles decreased, preventing the formation of dark matter particle-antiparticle pairs. Although annihilation continued, the number density of dark matter particles exponentially decreased. As the Universe expanded, the interaction eventually ceased, and the abundance of dark matter particles remained constant. The number density of dark matter particles after this "freeze-out" is called relic density.
The relic density serves as one of several observables well-suited for testing new models, and it is subsequently employed in this work. Current measurements of the relic density by the Planck space telescope [30] provide a value of

$$\Omega_{\mathrm{DM}} h^2 = 0.120 \pm 0.001\,. \tag{2.28}$$

Chapter 3

Scotogenic Model

This chapter presents the T1-2-A' Scotogenic model, introducing its extensions to the SM and investigating the generation of neutrino masses. Furthermore, contributions to the anomalous magnetic moment of the muon and processes involving charged lepton flavour violation will be examined.

3.1 T1-2-A' Scotogenic model

The original Scotogenic model (greek: "created from darkness") was introduced in 2006 by Ernest Ma [12] as a straightforward extension of the Standard Model. This model introduces a new $\mathbb{Z}_2$ symmetry to the SM gauge group. It has the capability to generate small majorana neutrino masses and due to the new $\mathbb{Z}_2$ symmetry features a stable dark matter candidate.

In this work a variant called T1-2-A' scotogenic model is discussed. The nomenclature T1-2-A' was developed in [1], where it is derived from the classification system proposed by Restrepo et al. in their 2013 work [13]. It serves as an extension of the original T1-2-A model, addressing its lack of capacity to simultaneously account for the anomalous magnetic moment of the muon, processes involving charged lepton flavor violation, and neutrino masses. Consequently, the model has been enhanced by the inclusion of an additional singlet fermion, which is denoted by the prime symbol.

In the Scotogenic model new added particles are all odd under the new $\mathbb{Z}_2$ symmetry and can be found in Table 3.1, while all SM particles are even under this symmetry. The scalar sector is extended with a $SU(2)$ singlet S and a doublet η. The fermion sector is extended by two $SU(2)$ singlets $F_{1,2}$ and two Weyl fermion doublets $\Psi_{1,2}$ having opposite hypercharge.

	$SU(3)_c$	$SU(2)_L$	$U(1)_Y$	$\mathcal{Z}_2$
η	1	2	1	−
S	1	1	0	−
$F_{1,2}$	1	1	0	−
Ψ_1	1	2	−1	−
Ψ_2	1	2	1	−

Table 3.1: Additional particle content of the T1-2-A' model. All new fields are odd under $\mathbb{Z}_2$. There is one additional $SU(2)_L$ doublet scalar η and one additional singlet scalar S. In the Fermionic sector there are two additional singlets $F_{1,2}$ and two doublet Weyl fermions $\Psi_{1,2}$.

3.1.1 Scalar sector

The scalar doublet η has the same quantum numbers as the Higgs field H, except for the $\mathbb{Z}_2$ symmetry. Because electroweak symmetry breaking (EWSB) exclusively involves the Higgs doublet, only the Higgs acquires a vacuum expectation value (vev). Therefore subsequent to the EWSB the scalar doublets can be expanded into their components as follows

$$H \;=\; \begin{pmatrix} G^+ \\ \frac{1}{\sqrt{2}}\big[v + h^0 + iG^0\big] \end{pmatrix}, \qquad \eta \;=\; \begin{pmatrix} \eta^+ \\ \frac{1}{\sqrt{2}}\big[\eta^0 + iA^0\big] \end{pmatrix}. \tag{3.1}$$

Here, h^0 is the SM Higgs boson, $v = \sqrt{2}\langle H\rangle \approx 246$ GeV denotes the vev and G^0 and G^+ are the would-be Goldstone bosons, that get absorbed by Z and W bosons. Moreover, η^0 and A^0 are CP-even and CP-odd neutral scalars, and η^+ is a charged scalar.
The scalar potential of the model is given by

$$\begin{aligned} V_{\text{scalar}} \;=\; & M_H^2\big|H\big|^2 + \lambda_H\big|H\big|^4 + \frac{1}{2}M_S^2S^2 + \frac{1}{2}\lambda_{4S}S^4 + M_\eta^2\big|\eta\big|^2 + \lambda_{4\eta}\big|\eta\big|^4 \\ & + \frac{1}{2}\lambda_S S^2\big|H\big|^2 + \frac{1}{2}\lambda_{S\eta}S^2\big|\eta\big|^2 + \lambda_\eta\big|\eta\big|^2\big|H\big|^2 + \lambda'_\eta\big|H\eta^\dagger\big|^2 \\ & + \frac{1}{2}\lambda''_\eta\Big[\big(H\eta^\dagger\big)^2 + \text{h.c.}\Big] + \alpha\Big[SH\eta^\dagger + \text{h.c.}\Big]. \end{aligned} \tag{3.2}$$

The first two terms correspond to the SM part associated with the Higgs doublet H. Both new scalars S and η have a mass term and interactions with the Higgs doublet H. Additionally there is a trilinear coupling α involving all three scalars. For simplicity, both λ''_η and α are assumed to be real. Therefore all couplings are real. This assumption implies the absence of any mixing between the CP-odd state A^0 with the CP-even states η^0 and S. After EWSB, the typical minimisation relation in the Higgs sector

$$m_{h^0}^2 = -2M_H^2 = 2\lambda_H v^2, \tag{3.3}$$

enables the elimination of the mass parameter M_H^2 in favor of the Higgs self-coupling λ_H. A Higgs mass of $m_{h^0} = 125\,\text{GeV}$ leads to a tree level value of $\lambda_H \approx 0.13$. In the subsequent parameter search, wherein one-loop corrections are taken into account, the relation becomes more intricate, leading to a deviation in the value of λ_H. Consequently, it is included as a free parameter to appropriately fit the Higgs mass.

Scalar Masses

By inserting the scalar doublets (3.1) into the scalar potential (3.2), the masses of the BSM scalars after EWSB can be derived. The relevant terms contributing to the masses of the BSM scalars originate from the Lagrangian quadratic in S, η^0 and A^0. The resulting mass matrix of the neutral scalars in the basis $\{S, \eta^0, A^0\}$ is given by

$$\mathcal{M}_\phi^2 = \begin{pmatrix} M_S^2 + \frac{1}{2}v^2\lambda_S & v\alpha & 0 \\ v\alpha & M_\eta^2 + \frac{1}{2}v^2\lambda_+ & 0 \\ 0 & 0 & M_\eta^2 + \frac{1}{2}v^2\lambda_- \end{pmatrix} . \tag{3.4}$$

with the definition $\lambda_\pm = \lambda_\eta + \lambda'_\eta \pm \lambda''_\eta$. This Matrix can be diagonalized by an orthogonal matrix U_ϕ to get the mass eigenstates

$$\begin{pmatrix} \phi_1^0 \\ \phi_2^0 \\ \phi_3^0 \end{pmatrix} = U_\phi \begin{pmatrix} S \\ \eta^0 \\ A^0 \end{pmatrix} . \tag{3.5}$$

Note that the mass eigenstate ϕ_3^0 is the same as the CP-odd scalar A^0, because there is no mixing with the other neutral scalars. The corresponding squared masses at tree-level read as

$$\begin{aligned} m_{\phi_{1,2}^0}^2 &= \frac{1}{2}\left[M_S^2 + M_\eta^2 + \frac{1}{2}v^2\left(\lambda_S + \lambda_+\right) \mp \sqrt{\left[M_S^2 - M_\eta^2 + \frac{1}{2}v^2\left(\lambda_S - \lambda_+\right)\right]^2 + 4v^2\alpha^2} \right] , \\ m_{\phi_3^0}^2 &= M_\eta^2 + \frac{1}{2}v^2\lambda_- , \end{aligned} \tag{3.6}$$

where $m_{\phi_1^0} < m_{\phi_2^0}$. The tree-level mass of the charged scalars is given by

$$m_{\eta^\pm}^2 = M_\eta^2 + \frac{1}{2}v^2\lambda_\eta . \tag{3.7}$$

3.1.2 Fermion sector

The Lagrangian for the additional fermions reads

$$\begin{aligned} \mathcal{L}_{\text{fermion}} &= \mathrm{i}\Big(\overline{\Psi}_j\sigma^\mu D_\mu\Psi_j + \frac{1}{2}\overline{F}_j\sigma^\mu\partial_\mu F_j\Big) - \frac{1}{2}M_{F_{ij}}F_iF_j \\ &\quad - M_\Psi\Psi_1\Psi_2 - y_{1i}\Psi_1 H F_i - y_{2i}\Psi_2\tilde{H}F_i \\ &\quad - g_\Psi^k\Psi_2 L_k S - g_{F_j}^k\eta L_k F_j - g_R^k e_k^c\tilde{\eta}\Psi_1 + \text{h.c.} \end{aligned} \tag{3.8}$$

with $i,j = 1,2$ and $k = 1,2,3$. L_k and e_k^c denote the left-handed and right-handed leptons, respectively. Moreover, the notation $\tilde{\phi} = i\sigma_2\phi^*$ is introduced for $\phi = H, \eta$. The fermionic Lagrangian comprises not only kinematic and mass terms but also Yukawa like couplings (y_{ij}) for the BSM fermions. Additionally, there are Yukawa like couplings (g) linking SM leptons to a BSM scalar and fermion, respectively. Eventhough these are not actual Yukawa couplings, they will be refered to as yukawa couplings in the following. For the singlet masses, one can always find a basis where $M_{F_{ij}}$ is diagonal. Therefore the notation can be simplified by setting $M_i = M_{F_{ii}}$ for $i = 1,2$. Moreover, it is assumed that $|M_1| \leq |M_2|$.

Fermion masses

For the masses of the fermions the $SU(2)_L$ representation of the Weyl Fermions

$$\Psi_1 = \begin{pmatrix} \Psi_1^0 \\ \Psi_1^- \end{pmatrix}, \qquad \Psi_2 = \begin{pmatrix} \Psi_2^+ \\ -\Psi_2^0 \end{pmatrix}, \tag{3.9}$$

is inserted into the Lagrangian (3.8). After EWSB, one gets four neutral fermions with the corresponding mass matrix in the Basis $\{F_1, F_2, \Psi_1^0, \Psi_2^0\}$

$$\mathcal{M}_\chi = \begin{pmatrix} M_1 & 0 & \frac{v}{\sqrt{2}}\, y_{11} & \frac{v}{\sqrt{2}}\, y_{21} \\ 0 & M_2 & \frac{v}{\sqrt{2}}\, y_{12} & \frac{v}{\sqrt{2}}\, y_{22} \\ \frac{v}{\sqrt{2}} y_{11} & \frac{v}{\sqrt{2}}\, y_{12} & 0 & M_\Psi \\ \frac{v}{\sqrt{2}} y_{21} & \frac{v}{\sqrt{2}} y_{22} & M_\Psi & 0 \end{pmatrix}. \tag{3.10}$$

This matrix can be diagonalized by a unitary matrix U_χ, giving the four mass eigenstates

$$\begin{pmatrix} \chi_1^0 \\ \chi_2^0 \\ \chi_3^0 \\ \chi_4^0 \end{pmatrix} = U_\chi \begin{pmatrix} F_1 \\ F_2 \\ \Psi_1^0 \\ \Psi_2^0 \end{pmatrix}, \tag{3.11}$$

with the eigenvalues m_{χ_i} ordered in the convention $m_{\chi_i} \leq m_{\chi_j}$ for $i < j$. Additionally there is one charged lepton of the form $\chi^- = (\Psi_1^-, \bar{\Psi}_2^-)^T$, using the convention $\bar{\Psi}_2^- = (\Psi_2^+)^\dagger$ with mass $m_\chi^- = M_\Psi$.

3.2 Generation of neutrino masses, the anomalous magnetic moment of the muon and CLFV processes

The following effects are generated at one-loop level and can be modeled by using effective operators. An effective operator or effective theory is an approximation to describe the

behavior of a system at a lower energy scale. The key concept is that at lower energies, certain degrees of freedom may become irrelevant, and their effects can be effectively encoded in terms of a smaller set of fields and parameters. Effective theories work best when there is a large gap between the energy scale of interest and the energy scale of the underlying dynamics. The four-fermion interaction proposed by Enrico Fermi in 1933 is one of the best-known effective field theories. It described the beta decay as a point like interaction between the four involved fermions and therefore serves as a low energy limit of the weak force.

3.2.1 Neutrino masses

To generate neutrino masses it is practical to introduce a vev to the neutrinos through interactions with the Higgs field. But it must be taken care of, that the neutrino mass is sufficiently small, to agree with current measurements ($m_{\nu_{\bar{e}}} < 0.8$ eV/c^2 [21]).
Because the new scalars in the T1-2-A' model do not acquire a vev the lowest order operator generating neutrino masses is the five dimensional Weinberg operator

$$\mathcal{O}_{\mathrm{WB}} \;=\; LLHH\,. \tag{3.12}$$

This higher dimensional operator is suppressed by a high energy scale Λ^0, leading to naturally small neutrino masses proportional to v^2/Λ^0. At tree level there are three realizations of this operator. The Seesaw mechanism type I,II and III, distinguished by the new mediating particle. In the present case, the $\mathbb{Z}_2$ symmetry forbids tree level diagrams. Therefore neutrino masses are generated radiatively through one loop diagrams. There are seven different diagrams (depicted in the appendix Figure A.2), which can be differentiated into three categories depending on the yukawa couplings g. There are two diagrams $\propto g_F^2$ and $\propto g_F g_\Psi$ each, and three diragrams $\propto g_\Psi^2$.
One example ($\propto g_F^2$) is shown on the left in Figure 3.1. The Leptons L interact with the majorana fermions F_i and the doublet scalars η through the new yukawa coupling g_F. To complete the fermion line a majorana mass term is inserted. The new scalars η complete via the coupling λ''_η with the Higgs doublet H.
After EWSB, the Higgs contributes its vev and there is only one type of diagram left depicted on the right hand side of Figure 3.1. It contains a loop consisting of a neutral scalar ϕ_k^0 with $k = \{1, 2, 3\}$ and a neutral fermion χ_j with $j = \{1, 2, 3, 4\}$. To calculate the majorana mass matrix the loop in the diagram has to be calculated. This calculation is done after EWSB with the new couplings $\lambda^\alpha_{j,k}$. Because $p^2 = m_\nu^2$ and the mass of the neutrinos is very small compared to the masses of the neutral scalars and fermions, the calculation can be viewed in the limit $p \to 0$. With this simplification the neutrino mass

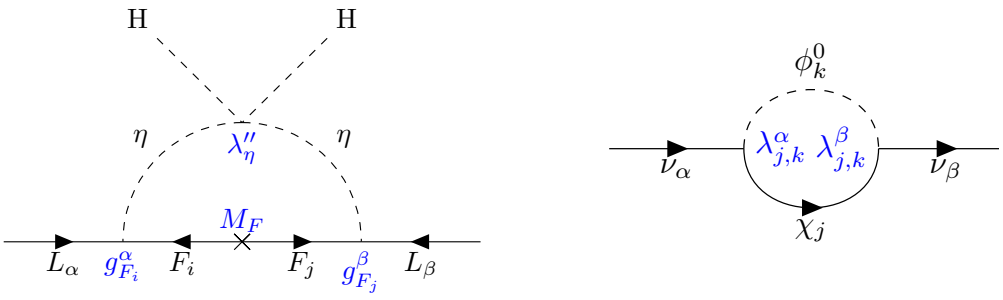

Figure 3.1: Neutrino mass generation in the T1-2-A' Scotogenic model. The vertex factors are added in blue. Left side represents one example of the total seven possible diagrams in gauge basis depicted in the appendix A. Right side is the only type of diagram in the mass basis. The arrows indicate the flow of hypercharge (left) and electric charge (right).

matrix can be calculated

$$(m_\nu)_{\alpha\beta} = \frac{1}{16\pi^2}\sum_{j,k}\lambda^\alpha_{j,k}\lambda^\beta_{j,k}m_j B_0(0,m_j,m_k)\,, \tag{3.13}$$

with the two point function

$$B_0(0,m_0,m_1) = \frac{m_0^2}{m_0^2-m_1^2}\ln\left(\frac{m_1^2}{m_0^2}\right)\,. \tag{3.14}$$

To complete this calculation the $\lambda^\alpha_{j,k}$ couplings have to be determined from the original g couplings. This is done by rewriting the lagrangian (3.8) with the mixing in the scalar and fermionic sector (3.5, 3.11).

$$\begin{aligned}\mathcal{L} &= -g^\alpha_\Psi\nu_\alpha(U^\dagger_\chi)_{4j}(U^T_\phi)_{1k}\chi_j\phi^0_k \\ &\quad -\sum_{i=1}^{2}\left(g^\alpha_{F_i}\frac{1}{\sqrt{2}}\nu_\alpha(U^\dagger_\chi)_{ij}(U^T_\phi)_{2k}\chi_j\phi^0_k + g^\alpha_{F_i}\frac{\mathrm{i}}{\sqrt{2}}\nu_\alpha(U^\dagger_\chi)_{ij}(U^T_\phi)_{3k}\chi_j\phi^0_k\right) \\ &\overset{!}{=} \lambda^\alpha_{j,k}\nu_\alpha\chi_j\phi^0_k\,.\end{aligned} \tag{3.15}$$

From this it follows that the new couplings are described by:

$$\lambda^\alpha_{j,k} = -\left[g^\alpha_\Psi(U^\dagger_\chi)_{4j}(U^T_\phi)_{1k} + \sum_{i=1}^{2}g^\alpha_{F_i}\frac{1}{\sqrt{2}}(U^\dagger_\chi)_{ij}\left((U^T_\phi)_{2k}+\mathrm{i}\,(U^T_\phi)_{3k}\right)\right]\,. \tag{3.16}$$

Inserting the explicit couplings into (3.13) gives the mass matrix depending on the original couplings before EWSB and the neutral scalar and fermionic mixings. This neutrino mass matrix can be expressed as [1]:

$$m_\nu = G^T M_L G\,, \tag{3.17}$$

where G contains the yukawa couplings g_Ψ and $g_{F_{1,2}}$:

$$G = \begin{pmatrix} g_\Psi^1 & g_\Psi^2 & g_\Psi^3 \\ g_{F_1}^1 & g_{F_1}^2 & g_{F_1}^3 \\ g_{F_2}^1 & g_{F_2}^2 & g_{F_2}^3 \end{pmatrix} , \tag{3.18}$$

and M_L is a symmetric 3×3 Matrix containing the information of the loop function and the mixing of the neutral scalar and fermionic sector. The explicit entries read

$$(M_L)_{11} = \sum_{j,k} b_{jk} (U_\chi^\dagger)_{4j}^2 (U_\phi^T)_{1k}^2 , \tag{3.19}$$

$$(M_L)_{12} = (M_L)_{21} = \frac{1}{\sqrt{2}} \sum_{j,k} b_{jk} (U_\chi^\dagger)_{1j} (U_\chi^\dagger)_{4j} (U_\phi^\dagger)_{1k} (U_\phi^T)_{2k} , \tag{3.20}$$

$$(M_L)_{22} = \frac{1}{2} \sum_{j,k} b_{jk} (U_\chi^\dagger)_{1j}^2 \left[(U_\phi^T)_{2k}^2 - (U_\phi^T)_{3k}^2 \right] , \tag{3.21}$$

$$(M_L)_{13} = (M_L)_{31} = \frac{1}{\sqrt{2}} \sum_{j,k} b_{jk} (U_\chi^\dagger)_{2j} (U_\chi^\dagger)_{4j} (U_\phi^T)_{1k} (U_\phi^T)_{2k} , \tag{3.22}$$

$$(M_L)_{23} = (M_L)_{32} = \frac{1}{2} \sum_{j,k} b_{jk} (U_\chi^\dagger)_{2j} (U_\chi^\dagger)_{1j} \left[(U_\phi^T)_{2k}^2 - (U_\phi^T)_{3k}^2 \right] , \tag{3.23}$$

$$(M_L)_{33} = \frac{1}{2} \sum_{j,k} b_{jk} (U_\chi^\dagger)_{2j}^2 \left[(U_\phi^T)_{2k}^2 - (U_\phi^T)_{3k}^2 \right] , \tag{3.24}$$

where $j = 1, 2, 3, 4$, $k = 1, 2, 3$ and the loop integrals are expressed in the functions

$$b_{jk} = \frac{1}{16\pi^2} \frac{m_{\chi_j^0}}{m_{\phi_k^0}^2 - m_{\chi_j^0}^2} \left[m_{\chi_j^0}^2 \ln\left(m_{\chi_j^0}^2 \right) - m_{\phi_k^0}^2 \ln\left(m_{\phi_k^0}^2 \right) \right] . \tag{3.25}$$

This mass matrix can then be diagonalized into the mass eigenstates and the eigenvalues represent the neutrino masses m_i, from which the corresponding mass squared differences can be calculated. In the Basis, where the SM lepton yukawa couplings are diagonal, the rotation matrix U_ν corresponds to the PMNS matrix from which the mixing angles and CP phase can be determined.

3.2.2 Anomalous magnetic moments and charged lepton flavour violating processes

The charged lepton flavour violating processes $l_\alpha \to l_\beta \gamma$ can be modeled with the effective operator

$$\mathcal{O} = L \sigma_{\mu\nu} e_R^c F^{\mu\nu} H , \tag{3.26}$$

where L and e_R^c are the left handed lepton doublet and the right handed lepton singlet respectively. H is the Higgs doublet. The field strength tensor $F^{\mu\nu}$ contains a photon

and is contracted with $\sigma_{\mu\nu} = \frac{i}{2}[\gamma_\mu, \gamma_\nu]$, where $[\gamma_\mu, \gamma_\nu]$ is the commutator of two gamma matrices γ_μ. This operator is called Wilson operator.
The following calculation regarding magnetic moments and the simple CLFV processes follows the approach of Crivellin et. al. [31]. With the Higgs contributing its vev, the effective Hamiltonian is given by

$$\mathcal{H} \;=\; c_R^{l_\beta l_\alpha} \bar{l_\beta} \sigma_{\mu\nu} P_R l_\alpha F^{\mu\nu} \;+\; \text{h.c.}\,, \tag{3.27}$$

where $c_R^{l_\beta l_\alpha}$ is a so called Wilson coefficient and P_R is the right projection operator. Note, that the vev is absorbed into the Wilson coefficient $c_R^{l_\beta l_\alpha}$. From this Hamiltonian simple formulas for the anomalous magnetic moment and the CLFV processes for the two body decays can be derived

$$\begin{aligned} a_\alpha \;&=\; -\frac{2m_\alpha}{e}\left(c_R^{l_\alpha l_\alpha} + c_R^{l_\alpha l_\alpha *}\right) \;=\; -\frac{4m_\alpha}{e}\text{Re}\left[c_R^{l_\alpha l_\alpha}\right]\,, \\ \text{BR}[l_\alpha \to l_\beta \gamma] \;&=\; \frac{m_\alpha}{4\pi\Gamma_{\text{tot}}(l_\alpha)}\left(|c_R^{l_\alpha l_\beta}|^2 + |c_R^{l_\beta l_\alpha}|^2\right)\,. \end{aligned} \tag{3.28}$$

where e is the elementary charge. In a general BSM model with new fermions Ψ and new scalars Φ the general lagrangian can be expressed in the form

$$\mathcal{L} \;=\; \bar{\Psi}\left(\Gamma_{\Psi\Phi}^{\alpha L} P_L + \Gamma_{\Psi\Phi}^{\alpha R} P_R\right) l_\alpha \Phi^* + \text{h.c.}\,, \tag{3.29}$$

where l_α are the SM leptons and $\Gamma_{\Psi\Phi}^{\alpha L}$ the new couplings. From this all BSM contributions to the Wilson coefficients can be expressed as

$$\begin{aligned} c_R^{l_\alpha l_\beta} \;&=\; \frac{e}{16\pi^2}\frac{M_\Psi}{M_\Phi^2}\Gamma_{\Psi\Phi}^{\beta L *}\Gamma_{\Psi\Phi}^{\alpha R}\left[f\left(\frac{M_\Psi^2}{M_\Phi^2}\right) + Qg\left(\frac{M_\Psi^2}{M_\Phi^2}\right)\right] \\ &+\; \frac{e}{16\pi^2}\frac{1}{M_\Phi^2}\left(m_\alpha \Gamma_{\Psi\Phi}^{\beta L *}\Gamma_{\Psi\Phi}^{\alpha L} + m_\beta \Gamma_{\Psi\Phi}^{\beta R *}\Gamma_{\Psi\Phi}^{\alpha R}\right)\left[\tilde{f}\left(\frac{M_\Psi^2}{M_\Phi^2}\right) + Q\tilde{g}\left(\frac{M_\Psi^2}{M_\Phi^2}\right)\right]\,, \end{aligned} \tag{3.30}$$

where Q is the electric charge of Ψ and M_Φ, M_Ψ are the masses of the BSM scalars and fermions, respectively. The explicit form of the loop functions f, g, $\tilde{f}$ and $\tilde{g}$ can be found in equation (B.1) in the appendix. Since this holds true for all BSM models, the only challenge is to find the model specific coefficients Γ.
The dominant contributions in the T1-2-A' model stem from the diagrams depicted in Figure 3.2. The left side is represented in the gauge basis, while the right side is expressed in the mass basis following EWSB. In the upper diagram, the fermion line is linked through the mass term M_Ψ, and the scalar line is connected via the trilinear coupling α. In the lower diagram, the singlet fermion F_i couples with Ψ_1 and the Higgs, whereas the scalar η establishes a direct link with the leptons. The key distinction lies in the coupling to the left-handed fermion doublet: it is g_Ψ in the upper diagram and g_F in the lower diagram. The $F^{\mu\nu}$ field can couple to any field with non zero hypercharge.

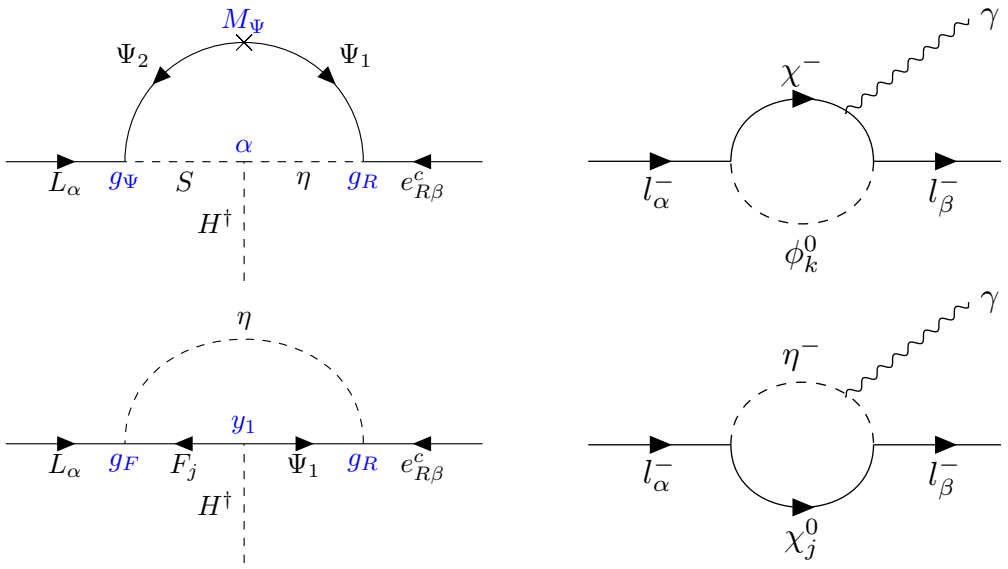

Figure 3.2: Dominant contributions to the anomalous magnetic moment of the muon and the charged lepton flavour violating processes. The vertex factors are added in blue. Left side is in gauge basis. Right side is in mass basis after EWSB. The arrows indicate the flow of hypercharge (left) and electric charge (right). In the left diagrams the $F^{\mu\nu}$ field can couple to any field with a non zero charge.

After EWSB, particles are depicted in the mass basis and form the diagrams on the right in Figure 3.2. In the upper diagram the majorana fermions Ψ_i provide a charged fermion χ^-, the Higgs contributes its vev and and due to the scalar singlet S the bottom line yields a neutral scalar ϕ^0_k, resulting in the top right diagram. In the lower diagram the scalar doublet η provides a charged scalar η^- and the neutral fermion χ^0_j stems from the singlet F_j connecting the fermion line, resulting in the diagram in the bottom right.
The top diagram yields the coefficients

$$\Gamma^{\alpha L}_k = -g^\alpha_\Psi (U^T_\phi)_{1k} \tag{3.31}$$

$$\Gamma^{\beta R}_k = -g^\beta_R \frac{1}{\sqrt{2}} (U^T_\phi)_{2k} + g^\beta_R \frac{\mathrm{i}}{\sqrt{2}} (U^T_\phi)_{3k} \,. \tag{3.32}$$

For the bottom diagram the coefficients are given by

$$\Gamma^{\alpha L}_j = -\sum_i^2 g^\alpha_{F_i} (U^\dagger_\chi)_{ij} \tag{3.33}$$

$$\Gamma^{\beta R}_j = -g^\beta_R (U^\dagger_\chi)_{3j} \,. \tag{3.34}$$

From this the Wilson coefficients can be determined and therefore the anomalous magnetic moment and the Branching ratios for $l_\alpha \to l_\beta \gamma$.

In this model there are also processes involving four leptons $l_\alpha \to l_\beta l_\gamma l_\delta$, which have strong experimental constraints. The calculation of these processes follows Ernesto Arganda et al. [32].

The fundamental processes involve penguin diagrams, wherein the photon couples with the charged fermion χ^- or scalar η^- in the loop, as illustrated in Figure 3.2 right, resulting in a lepton-antilepton pair. Furthermore, this intermediary photon can be substituted with a Z^0 boson , giving rise to supplementary diagrams. Moreover, the neutral fermion χ_j^0 or scalar ϕ_k^0 in the loop can couple to the Higgs, which can then aswell produce a lepton-antilepton pair. Additionally, box diagrams incorporate either a charged scalar and neutral fermion or a neutral scalar and charged fermion, contributing further to the overall process. All these processes contribute to the four lepton decay $l_\alpha \to l_\beta l_\gamma l_\delta$.

Additional constraints come from Z^0 decays into two different charged leptons. For these processes $Z^0 \to l_i^\pm l_j^\mp$ one part can be derived from the diagrams in Figure 3.2 where the Z^0 boson couples to the charged fermion χ^- or scalar η^- in the loop, resulting in two leptons of different flavour. Moreover, because the Z^0 boson couples differently to left and right handed fermions, additional contributions have to be considered.

The $\mu \to e$ conversion process occurring at the cores of titanium (Ti), lead (Pb), and gold (Au) is once again depicted by the diagrams presented in Figure 3.2. In this scenario, the photon or Z^0 boson interacts with the atomic nucleus of the corresponding elements. Contrary, the diagrams involving the Higgs connecting the neutral scalar or fermion in the loop to the atomic nucleus are significantly suppressed. Additionally there are no box diagrams, as the BSM particles do not couple to the quarks. Consequently, the conversion rate $\mathrm{CR}_{\mu\to e}(E)$ for $E = \{\mathrm{Ti}, \mathrm{Pb}, \mathrm{Au}\}$ can be determined from the dominant processes.

Chapter 4

Algorithms NSGA-III and CMA-ES

With the goal of exploring the parameter space of the T1-2-A' model using the NSGA-III and CMA-ES algorithms, this chapter provides an introduction to these optimization techniques. Beginning with fundamental principles of evolutionary algorithms, followed by an in-depth presentation of the single-objective algorithm, CMA-ES. Additionally, the concepts of Pareto improvement and non-dominated fronts are introduced, and subsequently applied to explain the NSGA-III algorithm. Finally, the adaptation of these algorithms for the T1-2-A' Scotogenic model is described and the MCMC scan from the previous work by Alvarez et al. [1] is introduced.

4.1 Introduction to Evolutionary algorithms

To explore the parameter space of the scotogenic model and find suitable parameter sets, evolutionary algorithms are employed. Evolutionary algorithms are a class of optimization algorithms inspired by the principles of biological evolution. They mimic the process of natural selection to iteratively improve solutions to complex problems. In each generation, a population of these candidate solutions undergoes selection, crossover (mating), and mutation operations to produce a new generation of potential solutions. Over time, these algorithms converge towards optimal or near-optimal solutions. Due to the close connection to biological evolution, solutions are referred to as individuals and a set of solutions as a population.
In this thesis two kinds of evolutionary algorithms are employed. One kind of evolutionary algorithms are genetic algorithms (GA), e.g. NSGA-III. And the other kind is Evolutionary strategy (ES), e.g. CMA-ES. The fundametnal flow of genetic algorithm consists of four steps:

- Calculate fitness for each individual
- Select best individuals

- Generate new population using Crossover (mating)
- Mutation

Firstly, the algorithm calculates the fitness of a each individual in the population. Following this, it selects the most promising individuals for reproduction. Thirdly, it generates new individuals through a combination of crossover and mutation, resulting in offspring with potential improvements. Lastly, the algorithm replaces parts or the entire population with this new generation of offspring. This iterative process continues until a predefined convergence criterion is achieved. Ideally, this can result in offspring that inherit and combine the strengths exhibited by both parents. Mutation plays a crucial role in the exploration of parameter spaces to generate traits beyond those already inherent within the existing population.

For crossover there is one important operator called simulated binary crossover (SBX) [33, 34]. This operator involves taking two parents and producing two offspring individuals. The key characteristic of the offspring is that the average of their genes is the same as the average of the parental genes. Incorporating the crowding degree parameter η_c, this operator utilizes a random distribution. The random number drawn from this distribution determines how similar the offspring is to the parents. A higher value of η_c tends to result in offspring closely resembling the parents, while a lower value of η_c leads to greater dissimilarity among individuals. For details see appendix C. The crossover operation is usually done step by step, taking two individuals off the parent population into the offspring population and apply the crossover operation based on the crossover probability.

For mutation the polynomial mutation [35] will be important. It utilizes a polynomial distribution to perturb the gene of an individual in its vicinity. The perturbation is regulated by a crowding degree denoted as η_m. Similar to the simulated binary crossover, an elevated η_m leads to minor deviations, whereas a higher value of η_m induces a more pronounced mutation. For details see appendix C. In genetic algorithms, the mutation of an individual is determined by a mutation probability. Subsequently, each gene of this individual undergoes mutation based on a specific probability known as the individual mutation probability. This value is typically small (~ 1) and signifies, on average, the amount of genes that undergo mutation.

The polynomial mutation operator is crafted to be constrained within a specified interval, preventing the generation of mutations outside that range. A similar constraint can be applied to the SBX operator.

In evolutionary strategies, the fundamental process shares similarities with genetic algorithms (GAs), involving fitness determination and selection. However, the generation of the subsequent population does not strictly rely on crossover and mutation mechanisms. In the case of Covariance Matrix Adaptation Evolution Strategy, for instance, the

succeeding generation is sampled from an iteratively adapted covariance matrix.
Evolutionary algorithms are versatile and can be applied to a wide range of problem types. Especially, not needing derivatives is an advantage when dealing with non-differentiable or non-continues objective functions. However, they can get computationally expensive when dealing with high numbers of populations or generations. Furthermore the performance is highly dependent on hyperparameters and finding the right set of hyperparameters can be challenging.

4.1.1 Covariance Matrix Adaptation Evolution Strategy (CMA-ES)

The Covariance Matrix Adaptation Evolution Strategy (CMA-ES) is a second-order approach that estimates the positive definite covariance matrix of the multivariate normal distribution through an iterative procedure. The approach follows a maximum-likelihood principle, aiming to enhance the probability of successful candidate solutions. The mean of the distribution is iteratively updated to maximize the likelihood of previously successful candidate solutions. Simultaneously, the covariance matrix of the distribution undergoes incremental updates to increase the likelihood of previously successful search steps. Thereby approximating the inverse Hessian matrix. Furthermore, the trajectory of the distribution mean is documented as evolution paths. These paths capture crucial information about the correlation between consecutive steps.
The standard CMA-ES algorithm is designed for single-objective optimization. However, for the given problem the requirement arises for a methodology capable of handling multiple objectives. This is elaborated on in section 4.2.
The algorithm depicted below follows the methodology outlined by Nikolaus Hansen [36]. CMA-ES follows the basic principles of evolutionary algorithms. An offspring generation, denoted as $g+1$, is generated by sampling $\lambda \geq 2$ individuals from a multivariate normal distribution. The fundamental equation from which the individuals $\boldsymbol{x}_i^{(g+1)}$ are sampled is as follows:

$$\boldsymbol{x}_i^{(g+1)} \sim \boldsymbol{m}^{(g)} + \sigma^{(g)} \mathcal{N}\left(0, \mathbf{C}^{(g)}\right) \qquad \text{for } i = 1, \ldots, \lambda\,, \tag{4.1}$$

Here, $\mathcal{N}\left(0, \mathbf{C}^{(g)}\right)$ describes a multivariate normal distribution with a mean of zero and a covariance matrix $\mathbf{C}^{(g)}$ at generation g. $\boldsymbol{m}^{(g)}$ represents the mean of the distribution, and $\sigma^{(g)}$ is the step size at generation g. For the multivariate normal distribution follows that

$$\begin{aligned} \mathcal{N}\left(\boldsymbol{m}, \sigma^2 \mathbf{C}\right) &\sim \boldsymbol{m} + \sigma\, \mathcal{N}\left(0, \mathbf{C}\right) \\ &\sim \boldsymbol{m} + \sigma\, \mathbf{C}^{\frac{1}{2}} \mathcal{N}\left(0, \mathbf{I}\right)\,. \end{aligned} \tag{4.2}$$

As is typical in evolutionary algorithms, the fitness of each individual is determined based

on the given problem.

$$f_i \;=\; f\left(\boldsymbol{x}_i^{(g+1)}\right) \qquad \text{for } i \;=\; 1,\ldots,\lambda\,, \tag{4.3}$$

and they are subsequently sorted $\boldsymbol{x}_{i:\lambda}^{(g+1)}$, where $i:\lambda$ denotes the individuals sorted by their fitness. To complete the evolutionary step the mean $\boldsymbol{m}^{(g+1)}$, the covariance matrix $\mathbf{C}^{(g+1)}$ and the step size $\sigma^{(g+1)}$ need to be determined for the next generation $g+1$.

Update Mean

The new mean $m^{(g+1)}$ is calculated as the weighted average of the best $\mu \leq \lambda$ individuals

$$\boldsymbol{m}^{(g+1)} \;=\; \sum_{i=0}^{\mu} w_i\, \boldsymbol{x}_{i:\lambda}^{(g+1)}\,, \tag{4.4}$$

where $\sum_{i=1}^{\mu} w_i = 1$ and $w_1 \geq w_2 \geq w_\mu > 0$. If $w_i = 1/\mu$, this results in a simple mean of the best μ points. This method introduces a basic selection mechanism as only the best μ individuals contribute. Furthermore, assigning different weights strengthens the contribution of better individuals. The final update generalizes the concept of weighted average (4.4) to

$$\boldsymbol{m}^{(g+1)} \;=\; \boldsymbol{m}^{(g)} + c_\mathrm{m} \sum_{i=0}^{\mu} w_i \left(\boldsymbol{x}_{i:\lambda}^{(g+1)} - \boldsymbol{m}^{(g)}\right)\,, \tag{4.5}$$

where c_m is the learning rate, commonly set to 1. For $c_\mathrm{m} \sum_{i=0}^{\mu} w_i = 1$, (4.5) resembles (4.4).

Adapting the Covariance Matrix

In the following is the full generational update of the covariance matrix divided into three parts

$$\mathbf{C}^{(g+1)} = \underbrace{(1 - c_1 - c_\mu \sum w_j)\; \mathbf{C}^{(g)}}_{\text{previous matrix}} + \underbrace{c_1\; \boldsymbol{p}_c^{(g+1)} \boldsymbol{p}_c^{(g+1)\mathsf{T}}}_{\text{rank-1 update}} + \underbrace{c_\mu \sum_{i=1}^{\lambda} w_i\; \boldsymbol{y}_{i:\lambda}^{(g+1)} \left(\boldsymbol{y}_{i:\lambda}^{(g+1)}\right)^{\mathsf{T}}}_{\text{rank-}\mu\text{ update}}, \tag{4.6}$$

where c_1, c_μ are the learning rates for rank-1 and rank-μ updates respectively. The first part describes the influence of the previous covariance matrix. In the following the rank-1 and rank-μ update are discussed.

The rank-μ update works similar to the update of the mean, by estimating the variance of sampled steps $\boldsymbol{x}_{i:\lambda}^{(g+1)} - \boldsymbol{m}^{(g)}$ and incorporating weights

$$\mathbf{C}_\mu^{(g+1)} \;=\; \sum_{i=1}^{\lambda} w_i \left(\boldsymbol{x}_{i:\lambda}^{(g+1)} - \boldsymbol{m}^{(g)}\right) \left(\boldsymbol{x}_{i:\lambda}^{(g+1)} - \boldsymbol{m}^{(g)}\right)^{\mathsf{T}}\,. \tag{4.7}$$

This estimation is then used to update the Covariance matrix

$$\begin{aligned}\mathbf{C}^{(g+1)} &= (1 - c_\mu \sum w_j)\ \mathbf{C}^{(g)} + c_\mu \sum_{i=1}^{\lambda} \frac{w_i}{\sigma^{(g)^2}} \left(\boldsymbol{x}_{i:\lambda}^{(g+1)} - \boldsymbol{m}^{(g)}\right) \left(\boldsymbol{x}_{i:\lambda}^{(g+1)} - \boldsymbol{m}^{(g)}\right)^\intercal \\ &= (1 - c_\mu \sum w_j)\ \mathbf{C}^{(g)} + c_\mu \sum_{i=1}^{\lambda} w_i\ \boldsymbol{y}_{i:\lambda}^{(g+1)} \left(\boldsymbol{y}_{i:\lambda}^{(g+1)}\right)^\intercal , \end{aligned} \tag{4.8}$$

with $\boldsymbol{y}_{i:\lambda}^{(g+1)} = (\boldsymbol{x}_{i:\lambda}^{(g+1)} - \boldsymbol{m}^{(g)})/\sigma^{(g)}$.
Because the sign information is lost in the rank-μ update, $-\boldsymbol{y}(-\boldsymbol{y})^\intercal = \boldsymbol{y}\boldsymbol{y}^\intercal$, the rank-1 update utilizes the evolution path to generate the new covariance matrix. The evolution path $\boldsymbol{p}_c^{(g)}$ at generation g is generated from consecutive steps

$$\boldsymbol{p}_c^{(g+1)} = (1 - c_c)\boldsymbol{p}^{(g)} + \mathrm{N}\frac{\boldsymbol{m}^{(g+1)} - \boldsymbol{m}^{(g)}}{c_m \sigma^{(g)}} , \tag{4.9}$$

where N is a normalization factor, c_c is the learning rate of the evolution path, commonly set between $1/n$ an $1/\sqrt{n}$, and with $\boldsymbol{p}_c^{(0)} = 0$. From the evolution path (4.9) the rank-1 update of the covariance matrix is calculated as

$$\mathbf{C}^{(g+1)} = (1 - c_1)\ \mathbf{C}^{(g)} + c_1\ \boldsymbol{p}_c^{(g+1)} \boldsymbol{p}_c^{(g+1)^\intercal} . \tag{4.10}$$

Combining both rank updates produces (4.8), where the advantages of both approaches are combined. The rank-μ update efficiently leverages information from the entire population, important for larger populations. Additionally, the rank-1 update harnesses information about the correlation between generations through the utilization of the evolution path, making it particularly valuable for smaller populations.

Updating the step size

The matrix adaptation lacks the capability to control the overall scale of the distribution and can only re-scale in a single direction. This limitation hinders fast convergence. To address this issue, a step size σ is introduced to significantly boost the learning rate. In order to regulate the step size, an evolution path is employed, as previously done for updating the covariance matrix (see Equation (4.8)). Fortunately, this method can be applied independently of the covariance matrix update. To construct the evolution path the same principle as in (4.9) is used, but this time the conjugate evolution path is constructed

$$\boldsymbol{p}_\sigma^{(g+1)} = (1 - c_\sigma)\boldsymbol{p}_\sigma^{(g)} + \mathrm{N}\ \mathbf{C}^{(g)^{-\frac{1}{2}}} \frac{\boldsymbol{m}^{(g+1)} - \boldsymbol{m}^{(g)}}{c_m \sigma^{(g)}} . \tag{4.11}$$

Where $\mathbf{C}^{(g)^{-\frac{1}{2}}}$ re-scales the step $\boldsymbol{m}^{(g+1)} - \boldsymbol{m}^{(g)}$, so that the length of the evolution path is independent of its direction. To decide if the step size should be increased or decreased,

the length of the evolution path $\|\boldsymbol{p}_\sigma^{(g+1)}\|$ is compared with its expected length $\mathrm{E}\|\mathcal{N}(0,\mathrm{I})\|$. If the evolution path is long, single steps point towards the same direction, therefore the step size can be increased to cover the same distance in fewer steps. Conversely when the evolution path is short, steps counteract each other, indicating a lack of correlation, necessitating a reduction in step size. In summery if the evolution path is longer than its expected length the step size is increased and vice versa, giving the following update

$$\sigma^{(g+1)} = \sigma^{(g)} \exp\left\{\left(\frac{c_\sigma}{d_\sigma}\left(\frac{\|\boldsymbol{p}_\sigma^{(g+1)}\|}{\mathrm{E}\|\mathcal{N}(0,\mathrm{I})\|} - 1\right)\right)\right\}, \tag{4.12}$$

where $d_\sigma \approx 1$ is a dampening factor for the change in step size, and c_σ the learning rate. It turns out that the length of the evolutionary path serves as an intuitively and empirically well-validated metric for assessing the overall step length [36].
This concludes one generational update of the CMA-ES algorithm. On the one hand, it has only 3 hyperparameters making it cheap to tune. The hyperparameters are the population size, the initial stepsize and the maximum generations. It is also very robust to noise in the objective function making it suitable to complex objective spaces. On the other hand, CMA-ES can be very sensitive to the initial starting point and is only single objective which can be a disadvantage in multiobjective optimitation problems. Additionally, once a viable solutions is found, subsequent solutions tend to cluster closely around this point.

4.1.2 Pareto improvement and non-dominated sorting

Optimizing a problem for multiple objectives presents a challenging task, especially when these objectives conflict with one another. The following NSGA-III algorithm addresses this challenge by employing a technique known as non-dominated sorting to assess the fitness of a solution for multiple objectives.
Firstly, let's clarify the concept of Pareto improvement. In the context of our discussion, let's assume that solutions within the objective space have already been identified. A Pareto improvement refers to a transition from a solution B to another solution A, where at least one objective demonstrates improvement, while no other objective is worse off. In other words, A is said to dominate B if

$$\forall i \in \text{Objectives}, \quad A_i \leq B_i \quad \text{and} \quad \exists j \in \text{Objectives} \quad \text{such that} \quad A_j < B_j\,. \tag{4.13}$$

A solution A is considered Pareto optimal if no Pareto improvement can be made. The set of Pareto optimal solutions is called the Pareto optimal front or non-dominated front. In the two dimensional example depicted in Figure 4.1 (left), the blue solutions form the non-dominated front of the set of all solutions.

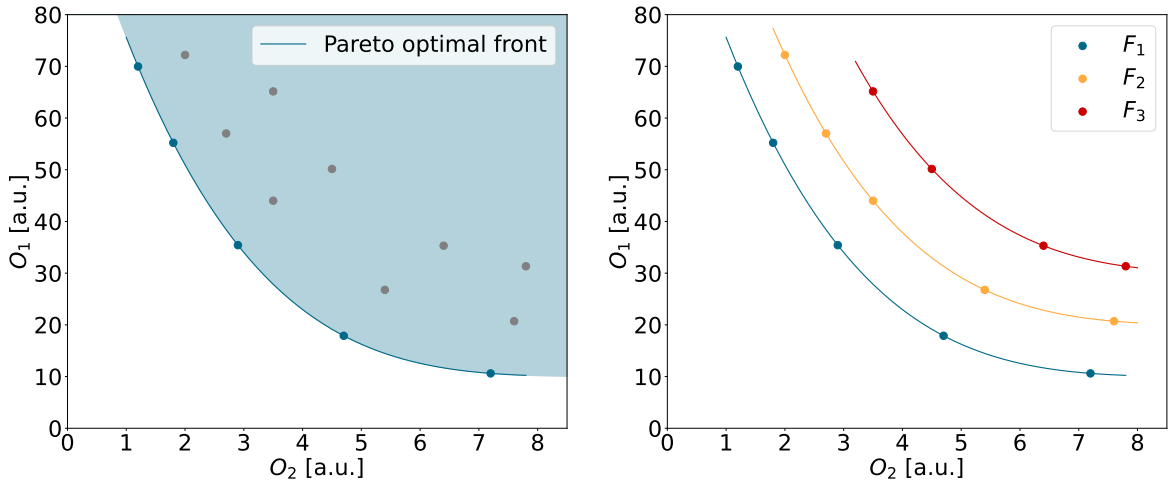

Figure 4.1: Pareto optimal front for a two dimensional example (left). Solutions assigned into non-dominated fronts (right).

To sort the solutions by non-dominated fronts, ranks are systematically assigned through an iterative process. Initially, the non-dominated front F_1 of the set S of all solutions is identified and designated rank 1. Subsequently, the solutions within front F_1 are excluded, and the non-dominated front F_2 of the remaining solutions in $S \setminus F_1$ is determined. This process is reiterated until all solutions are allocated to a non-dominated front. An example is depicted in Figure 4.1 (right), where all solutions have successfully been assigned to a non-dominated front.

4.1.3 Non-dominated Sorting Genetic Algorithm - III (NSGA-III)

The Non-dominated Sorting Genetic Algorithm - III (NSGA-III) is a modification of the NSGA-II [37] algorithm, to handle more than 3 objectives. They only differ in their diversity-preserving mechanisms. While NSGA-II is well-suited for 1 to 3 objectives, using a crowding distance approach, NSGA-III can handle 3 or more objectives due to its utilization of reference point selection, which is better suited for high dimensional objective spaces.

The following illustration of the algorithm follows the approach of Kalyanmoy Deb et al. [14]. The basic flow of both NSGA-II and NSGA-III follow the diagram depicted in Figure 4.2. The difference is that NSGA-III uses reference point sorting and NSGA-II utilizes the crowding distance at this selection step. To illustrate one generational step the nth generation is considered. The pseudo code for this algorithm can be found in the appendix D. Assume P_n is the parent population of size N, from which the Offspring population Q_n of size N is generated. This is accomplished by using crossover and mutation operations. specifically the simulated binary crossover and the polynomial mutation [33–

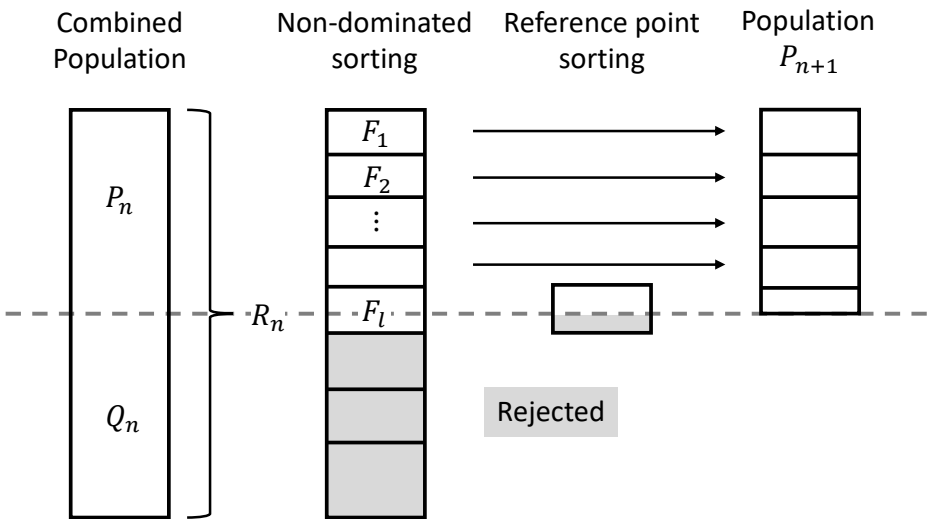

Figure 4.2: One generational update of the NSGA-III evolutionary algorithm [14].

35]. To acquire the next generation P_{n+1}, N individuals from the combined population $R_n = P_n \cup Q_n$ have to be selected. Therefore R_n is sorted by non-dominated ranks. These ranks are then successively selected until the size of P_{n+1} reaches N or surpasses N. In the former case the selection is finished. In most cases the last rank exceeds N individuals. For this last non-dominated front F_l a diversity preserving selection is used. Therefore reference points are defined in the objective space. These reference points serve as the basis for selecting diverse solutions of the last Front. The reference points are placed on a normalized hyper plane that intersects at one with all objectives. This is depicted for a three dimensional example in Figure 4.3. With p divisions across each objective and M objectives, the total number of reference points is given by

$$H = \binom{M+p-1}{p}. \tag{4.14}$$

To begin, individuals are first rescaled to the interval $[0, 1]$ in each objective. To associate individuals with reference points, reference lines are drawn between the origin and each reference point. The individuals are then assigned to the closest reference point by calculating the perpendicular distance. Consequently, each point can have one, many or no individual associated with it. Each point j is then assigned a niche count p_j based on how many individuals from the already selected fronts are associated with them. The reference points are then sorted by p_j and the lowest is picked. If there are multiple points with the same niche count p_j, one point is chosen at random. Now two cases have to be distinguished, $p_j = 0$ and $p_j \geq 1$

For $p_j = 0$ there can be two scenarios. One or more members of F_l are associated with j, in which case the one with the smallest distance is selected and the niche count is

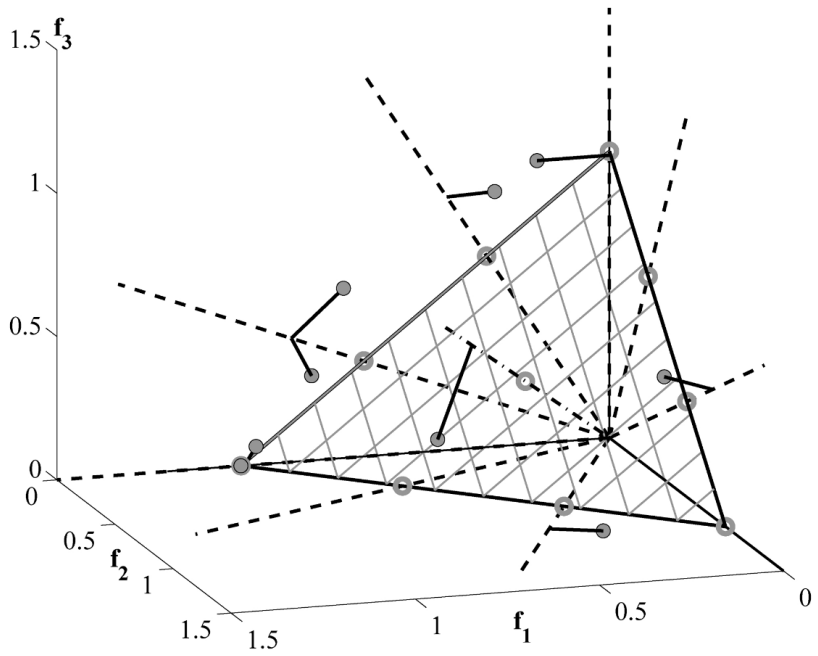

Figure 4.3: Association of individuals with the reference points. Taken from [14]

incremented. Second, there is no individual in F_l associated with j. In this case the reference point j is excluded from future searches for this generation.

For $p_j \geq 1$ a random individual from F_l, if exists, is selected and the niche count is incremented. This procedure is repeated until all empty spots in P_{n+1} are filled. This completes one generational update of the NSGA-III algorithm.

The algorithm incorporates elitism as the new population $P_{\mathrm{n+1}}$ is chosen from the combined population R_{n}. This ensures the survival of the best individuals. Additionally, the utilization of reference points and Pareto fronts emphasizes diversity in the objective space. Moreover, maintaining a high population number makes the algorithm more resilient and provides more global information. Furthermore, calculating the fitness of an individual is independent of other factors than the individual, making it easy to parallelize this algorithm.

However, NSGA-III has a high number (8) of hyperparameters compared to CMA-ES making it computationally more expensive to tune for a given problem. These hyperparameters are the population size, the maximum generations, the crossover probability, the crossover crowding degree, the mutation probability, the mutation crowding degree and the individual mutation probability. Moreover, NSGA-III only preserves diversity in the objective space, once the algorithm found a suitable solution, the population will converge around this point in the parameter space.

Parameter	Interval	mapping
λ_H	$[0.1; 0.3]$	lin
λ_{4S}, $\lambda_{4\eta}$	$[10^{-8}; 1]$	log
$\lambda_{S\eta}$, λ_S, λ_η, λ'_η, λ''_η	$[-1;-10^{-8}]$, $[10^{-8}; 1]$	bilog
α	$[-10^4;-1]$, $[1; 10^4]$	bilog
M_S^2, M_η^2	$[5 \times 10^5; 5 \times 10^6]$	lin
M_1, M_2	$[100; 2000]$	lin
M_Ψ	$[700; 2000]$	lin
y_{ij}, $(i,j = 1,2)$	$[-3; -10^{-8}]$, $[10^{-8}; 3]$	bilog
g_R^k, g_Ψ^k, $g_{F_j}^k$, $(k = 1,2,3)$, $(j = 1,2)$	$[-3; -10^{-8}]$, $[10^{-8}; 3]$	bilog

Table 4.1: Ranges for the input parameter. These are chosen to be comparable to the MCMC search [1]. All dimensional quantities are given in GeV. The red colored parameters are assumed to be complex and the interval is defined for the real and imaginary part.

4.2 Adapting NSGA-III and CMA-ES for the T1-2-A' model

The NSGA-III and CMA-ES algorithms are implemented in *Python* using the DEAP evolutionary computation framework [38]. The T1-2-A' model has already been implemented in SAHRA [39] to generate the code for SPheno [40, 41] and MicrOmegas [42]. SPheno computes the mass spectrum and low energy observables and MicrOmegas computes the dark matter relic density. The management of these modules is also handled through *Python*. The project's code is available in the repository [43].

To implement the evolutionary algorithms, first a genetic representation of the model parameters is needed. Examination of the Lagrangian equations (3.2) and (3.8) reveals the introduction of 14 real and 16 complex parameters in this model, as presented in Table 4.1. The complex parameters are represented by two real valued numbers for the real and imaginary parts, respectively. This gives a total of 46 real valued parameters. Incorporating these 46 parameters into the genetic algorithms involves representing each solution with an individual comprising 46 real-valued genes.

To simplify the calculations for evolutionary operations such as crossover and mutation, each individual is assigned both a phenotype and a genotype representation, each comprising 46 genes. he genotype representation is confined within a box space, where each gene g falls within the interval $[0, 1]$. All evolutionary operations take place within this box space.

The phenotype represents the actual physical values of the parameters. To establish the phenotype representation, a mapping from the genotype representation to the phenotype

representation is employed. To facilitate an effective scan these mappings are split into three kinds linear, logarithmic, or bilogarithmic.

$$\begin{aligned} P_{\text{lin}}(g) &= g_{\min} + \left(\frac{g_{\max} - g_{\min}}{b-a}\right)(g-a)\,, \quad \text{with} \quad a=0,\, b=1\,, \\ &= g_{\min} + (g_{\max} - g_{\min})\, g\,, \qquad (4.15) \\ P_{\log}(g) &= 10^{\log_{\min} + (\log_{\max} - \log_{\min})\, g}\,, \qquad (4.16) \\ P_{\text{bilog}}(g) &= \begin{cases} 10^{(\log_{\min} + (\log_{\max} - \log_{\min})\, 2\,(g-0.5))} & \text{if } g \geq 0.5 \\ -10^{(\log_{\min} + (\log_{\max} - \log_{\min})\ \ 2g)} & \text{if } g < 0.5 \end{cases}\,, \qquad (4.17) \end{aligned}$$

where g is the genotype representation, $\log_{\min} = \log(g_{\min})$ ($\log_{\max} = \log(g_{\max})$) and $g_{\min}$, $g_{\max}$ are the minimal and maximal values of the phenotype representation of the parameter, respectively. Logarithmic mappings are utilized to achieve an even distribution across different orders of magnitude, while the bilogarithmic mapping additionally accommodates negative values. Depending on the specific requirements for each parameter, one of these mappings is selected, as outlined in Table 4.1.

The parameter search in this study is compared with the prior work conducted by Alvarez et al. [1], therefore similar parameter ranges are adopted. These ranges remain consistent for all shared parameters, with the exception of the Yukawa couplings y_{ij} and g, which are assigned an expanded range to be able to explore novel regions in the parameter space. Furthermore, slight adjustments are made to the ranges for λ_{4S}, $\lambda_{4\eta}$, and λ_H.

As a next step the observables for an individual have to be calculated to determine its fitness. This involves employing the previously mentioned tools, namely SPheno and MicrOMEGAs. The observables are also refereed to as objectives or constraints. In total, there are 31 objectives, including the already discussed neutrino masses, mixing angles (including the charge parity phase), the anomalous magnetic moment of the muon, and the relic density of dark matter. Additionally, the Higgs mass is introduced as an objective, due to one-loop corrections to its mass. These objectives are displayed in Table 4.2 together with the uncertainties applied in this study. Note, that for the Higgs mass M_H and the relic density $\Omega_{CDM}h^2$ the theoretical uncertainties in this model are larger than the experimental ones, due to electroweak corrections and dark matter annihilation calculations. Consequently, the theoretical uncertainties are applied to them, whereas the remaining objectives incorporate the experimental uncertainties.

Furthermore, the upper limits of 22 relevant CLFV processes, presented in Table 4.3, are taken into account.

These observables form the basis for calculating the fitness of each individual. The fitness of an individual characterizes its validity, and this validity is determined by the proximity of its observables to the objectives in the objective space. Consequently, a cost function

Objective	Interval
M_H	125.25 ± 1.00 GeV
Δm_{21}	$7.42^{+0.21}_{-0.20} \cdot 10^{-5}\,\mathrm{eV}^2$
Δm_{31}	$2.517^{+0.026}_{-0.028} \cdot 10^{-3}\,\mathrm{eV}^2$
$\sin^2(\theta_{12})$	0.304 ± 0.012
$\sin^2(\theta_{13})$	$0.02219^{+0.00062}_{-0.00063}$
$\sin^2(\theta_{23})$	$0.573^{+0.016}_{-0.020}$
δ	$197^{+27}_{-24}\,^\circ$
Δa_μ	2.51 ± 0.59
$\Omega_{CDM}h^2$	0.12 ± 0.01

Table 4.2: Objectives for the parameter search: Higgs mass [25], neutrino data [20], anomalous magnetic moment of the muon [7] and dark matter relic density [30]. Note that the errors for the Higgs mass and the DM relic density are not the experimental errors, but estimations of theoretical uncertainties.

is computed as follows

$$C(\mathcal{O}) \;=\; \max(0, -\mathcal{O} + \mathcal{O}_{LB}, \mathcal{O} - \mathcal{O}_{UB})\,, \tag{4.18}$$

where $\mathcal{O}_{LB}$ and $\mathcal{O}_{UB}$ are the upper and lower bounds of the observable, respectively. For an observable outside the bounds, this function is positive $C(\mathcal{O}) > 0$. If the observable is within the bounds, signifying the agreement with the objective, the cost function is $C(\mathcal{O}) = 0$. Consequently finding valid points corresponds to minimising this cost function. The observables exhibit largely different magnitudes. In order to enhance comparability, the constraint function undergoes scaling through a logarithmic transformation, facilitating the comparison of observables of different magnitudes.

$$F_{\text{ind}}(\mathcal{O}) \;=\; \log_{10}\left(1 + C(\mathcal{O})\right)\,. \tag{4.19}$$

This scaling has an added advantage of introducing a numerical infinity, given that the maximum value for the fitness, using 64-bit floats, is approximately 700. This proves useful when handling parameter sets that produce unphysical results. In such cases, the fitness of the individual can be set to the maximum value, ensuring its exclusion from selection.

The fitness is computed for each observable, resulting in a 31-dimensional fitness vector. The NSGA-III algorithm is adept at utilizing this vector, given its design for handling multiple objectives. Conversely, the CMA-ES is fundamentally a single objective algorithm. There are several methods to deal with multiple objectives. Addressing this requirement involves combining multiple objectives into a single value. In this case through an arith-

Constraints	limit	Constraints	limit
$\mathrm{BR}[\mu^- \to e^-\gamma]$	$< 4.2 \cdot 10^{-13}$	$\mathrm{BR}[\tau^- \to e^-\eta]$	$< 9.2 \cdot 10^{-8}$
$\mathrm{BR}[\tau^- \to e^-\gamma]$	$< 3.3 \cdot 10^{-8}$	$\mathrm{BR}[\tau^- \to e^-\eta']$	$< 1.6 \cdot 10^{-7}$
$\mathrm{BR}[\tau^- \to \mu^-\gamma]$	$< 4.2 \cdot 10^{-8}$	$\mathrm{BR}[\tau^- \to \mu^-\pi]$	$< 1.1 \cdot 10^{-7}$
$\mathrm{BR}[\mu^- \to e^-e^+e^-]$	$< 1.0 \cdot 10^{-12}$	$\mathrm{BR}[\tau^- \to \mu^-\eta]$	$< 6.5 \cdot 10^{-8}$
$\mathrm{BR}[\tau^- \to e^-e^+e^-]$	$< 2.7 \cdot 10^{-8}$	$\mathrm{BR}[\tau^- \to \mu^-\eta']$	$< 1.3 \cdot 10^{-7}$
$\mathrm{BR}[\tau^- \to \mu^-\mu^+\mu^-]$	$< 2.1 \cdot 10^{-8}$	$\mathrm{CR}_{\mu\to e}(\mathrm{Ti})$	$< 4.3 \cdot 10^{-12}$
$\mathrm{BR}[\tau^- \to \mu^+e^-e^-]$	$< 1.5 \cdot 10^{-8}$	$\mathrm{CR}_{\mu\to e}(\mathrm{Pb})$	$< 4.3 \cdot 10^{-11}$
$\mathrm{BR}[\tau^- \to \mu^-e^+e^-]$	$< 1.8 \cdot 10^{-8}$	$\mathrm{CR}_{\mu\to e}(\mathrm{Au})$	$< 7.0 \cdot 10^{-13}$
$\mathrm{BR}[\tau^- \to \mu^-e^+\mu^-]$	$< 1.7 \cdot 10^{-8}$	$\mathrm{BR}(Z^0 \to e^\pm\mu^\mp)$	$< 7.5 \cdot 10^{-7}$
$\mathrm{BR}[\tau^- \to e^-\mu^+\mu^-]$	$< 2.7 \cdot 10^{-8}$	$\mathrm{BR}(Z^0 \to e^\pm\tau^\mp)$	$< 5.0 \cdot 10^{-6}$
$\mathrm{BR}[\tau^- \to e^-\pi]$	$< 8.0 \cdot 10^{-8}$	$\mathrm{BR}(Z^0 \to \mu^\pm\tau^\mp)$	$< 6.5 \cdot 10^{-6}$

Table 4.3: Constraints from the charged lepton flavour violating branching ratios or conversion ratios [25].

metic mean. This is conducted by initially rescaling the fitness values to lie within the interval [0,1] and subsequently summing them up.
Alternatively, there exists a dedicated multiobjective version of the CMA-ES algorithm, details in [44]. Although this variant was also applied to search the parameter space of the T1-2-A' model, it yielded no results. This is further discussed in chapter 5. Moreover, the standard CMA-ES algorithm had challenges to fit all objectives. This was addressed by introducing a hierarchy to the objectives, forcing the algorithm to first focus on one objective and subsequently, consider the other objectives. This lead to a great improvement and was termed h-CMA-ES. It is further elaborated on in chapter 5.
Through hyperparameter tuning using optuna [45] preferred sets of hyperparmeters where determined for both algorithms. For NSGA-III a population size of 400 was chosen, spanning a maximum of 2000 generations. The crossover operation was assigned a probability of 0.9 and a crowding degree of $\eta_c = 30$. For mutation, a probability of 0.5 was selected, along with a crowding degree of $\eta_m = 40$ and an individual mutation probability of 4.
For all variants of CMA-ES the population was set to 10 with an initial step size of $\sigma^{(0)} = 0.3$ and a maximum generation of 4000. This corresponds to a maximum of 40000 points calculated per run. Both algorithms are set to stop searching when at least 100 valid points are found.

The previous MCMC scan

The parameter search in this study is also compared to the previous work conducted by Alvarez et al. [1]. In their research, they employed a Markov Chain Monte Carlo approach.

To mitigate complexity and enhance computational efficiency, they adopted the Casas-Ibarra parametrization [16] for expressing the Yukawa couplings g_Ψ and g_{F_j} in terms of neutrino oscillation data. This approach ensures that, for any given parameter set, the neutrino data fits the measurements at least on tree level. The chosen CI parametrization method takes into account the generation of the anomalous magnetic moment of the muon, contributing to a reduction in the parameter space to a region with a high likelihood of discovering valid parameter sets. Respecting the constraints imposed by Δa_μ and CLFV processes, particularly the two-body decays $\mu \to e\gamma$, $\tau \to \mu\gamma$, and $\tau \to e\gamma$, establishes a hierarchy for the Yukawa couplings:

$$\begin{aligned} |g_\Psi^1| &\lesssim 10^{-5}\,, \\ |g_\Psi^2| &\sim 1\,, \\ |g_\Psi^3| &\lesssim 10^{-3}\,, \\ |g_{F_j}^\alpha| &\lesssim 10^{-3}\,, \quad \text{for} \quad \alpha = \{1,2,3\}\,,\ j = \{1,2\}\,. \end{aligned} \tag{4.20}$$

The coupling g_Ψ^2 must be sufficiently large to accommodate the anomalous magnetic moment of the muon. Conversely, the couplings for the other two lepton flavors need to be sufficiently small to satisfy the CLFV limits. In total, this reduces the parameter space to 20 free parameters, but also limits the search to a specific region. The MCMC scan performed 75 chains of 200 points each, where the initial 35 points were omitted to only keep points where the chains were well-initialized. Note that for this method not all points necessarily fit all objectives, however they are all close to the experimental bounds.
The MCMC scan utilized a modified CI parametrisation to reduce complexity, in contrast NSGA-III and CMA-ES handle the whole complexity of the T1-2-A' models parameter space. It is intriguing to compare the different results and ascertain if the new methods proposed in this work are viable to find parameter sets within this heightened complexity. Additionally, the analysis aims to determine the presence of regions in the parameter space that extend beyond those previously identified.

Chapter 5

Results

This chapter presents the results of the parameter space scan of the evolutionary algorithms NSGA-III and CMA-ES, respectively h-CMA-ES. The initial phase involves a random scan, followed by a comparison of the performance of NSGA-III and h-CMA-ES. Subsequently, an assessment of Yukawa couplings, CLFV processes, and DM candidates is conducted, drawing comparisons between NSGA-III h-CMA-ES and the previous MCMC scan by Alvarez et al. [1]. Finally, a brief analysis of LHC phenomenology is conducted.

5.1 Random scan

Firstly, a random scan of the parameter space was conducted to establish a baseline for comparison. In this process, 10^6 random points were evaluated. Despite the extensive scan, no point satisfying all objectives was identified. The percentage distribution of random points meeting a specific number of objectives is illustrated on the left in Figure 5.1, where the majority of points successfully satisfy 15 to 23 objectives simultaneously. Notably, a maximum of 26 objectives was achieved concurrently. Considering this, shows that finding a point through a random scan would require a few orders of magnitude more sampled points. The right side of Figure 5.1 provides a breakdown of the points from the random scan based on individual objectives. It is observed that most CLFV processes are relatively easy to satisfy, with the anticipated exception of $\mathrm{BR}(\mu \to e\gamma)$ and $\mathrm{BR}(\mu \to 3e)$ being the most challenging among them. Also the Conversion ratios $\mathrm{CR}_{\mu\to e}$ where more difficult to fit. Additionally, other objectives such as neutrino data, a_μ, and dark matter relic density were predictably more challenging to accommodate.

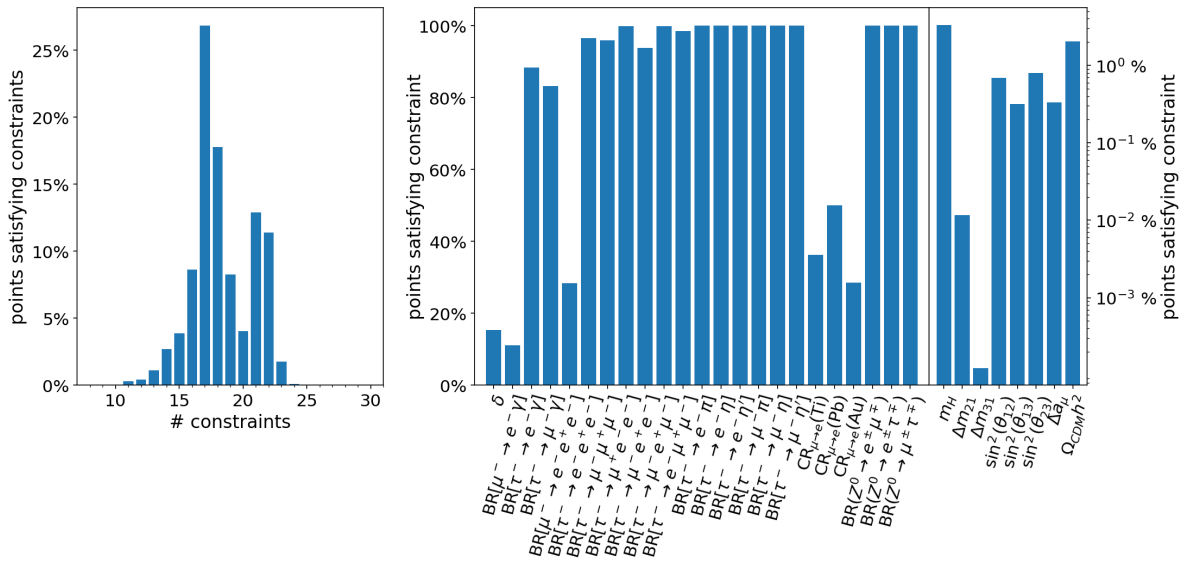

Figure 5.1: Percentage of points generated by the random scan, satisfying a specific number of constraints simultaneously (left). Percentage of points satisfying each constraints divided into a linear and logarithmic part (right).

5.2 General results

Initially $\mathcal{O}(10^2)$ iterations of the CMA-ES algorithm produced unsatisfactory outcomes, with only a 3% convergence rate. The basic implementation of CMA-ES of the algorithm lacks efficiency in handling all constraints simultaneously. Notably, the algorithm consistently fitted all but one objective: the anomalous magnetic moment of the muon. Due to the inherent challenge posed by fitting Δa_μ, an enhancement is proposed through the introduction of a hierarchical structure to the observables. This restructuring of the fitness evaluation comprises that if the objective Δa_μ is met, the fitness is calculated conventionally. However, if Δa_μ is not satisfied, all other observables are assigned the maximum fitness, resembling a severely bad fit, as the fitness metric is geared towards minimization. This improved methodology, termed the hierarchical CMA-ES (h-CMA-ES), initially prioritizes the anomalous magnetic moment of the muon before addressing the remaining objectives. Implementing this modification significantly raises the convergence rate to approximately 12%, which makes this approach much more practical.

The NSGA-III algorithm encountered challenges in satisfying the anomalous magnetic moment of the muon, as well. Despite these difficulties, the algorithm successfully identified valid points, demonstrating a convergence rate of 29%.

Since CMA-ES converged relatively fast and NSGA-III has a high convergence rate, a multiobjective CMA-ES (MO-CMA-ES) scan was implemented, which could potentially combine the fast convergence of CMA-ES and the higher convergence rate of NSGA-III. Unfortunately this approach did not yield any results as MO-CMA-ES did not converge at

all. One problem could be, that the MO-CMA-ES was only tested with lower population numbers $\mathcal{O}(10)$, so increasing this hyperparameter could greatly increase the success, but at a cost of much more computations per valid point, which in turn could make it less efficient than the other two algorithms.
The two successful algorithms NSGA-III and h-CMA-ES found 14694 and 7220 valid points for $71.2 \cdot 10^6$ and $23.96 \cdot 10^6$ evaluated points respectively. This corresponds to 1:4846 and 1:3319 valid points per sampled point respectively. Compared to the random scan this is at least 200 times better than a random scan. Note that the random scan did not find any valid points, making this the absolute lower bound, with the actual improvement beeing some orders of magnitude higher. The difference in the number of sampled points for NSGA-III and h-CMA-ES results from issues with the HPC cluster (High Performance Computing), which the calculations were performed on and the usable computing capacities.
In general, h-CMA-ES exhibits a more concentrated focus in individual runs, where points closely cluster within each run. However, the outcomes of distinct runs display a broader dispersion. In contrast, NSGA-III demonstrates a heightened distribution within individual runs, but emphasizing a more pronounced concentration to a specific parameter regions across different runs. Notably, NSGA-III tends to form patterns wherein one parameter remains relatively constant while others vary, resulting in recognizable lines or crosses in the plots. This characteristic is visible in most plots of the valid parameter sets. Consequently, it can be inferred that h-CMA-ES provides a more comprehensive coverage of the parameter space in comparison to NSGA-III. But compared to the MCMC scan both NSGA-III and h-CMA-ES provide a worse coverage for the shared region of the parameter space.
This difference of NSGA-III and h-CMA-ES can also be seen in the λ couplings and the mass parameters in the scalar sector. A selection is displayed in Figure E.1 in the appendix.

5.3 Comparison of NSGA-III, h-CMA-ES and MCMC

In the following, the results obtained from the three distinct approaches: NSGA-III, h-CMA-ES, and MCMC [1], are compared, focusing on crucial parameters such as the Yukawa couplings, processes involving charged lepton flavor violation, and dark matter. The MCMC analysis yielded 12,375 ”valid” points. It is noteworthy that not every point generated by MCMC necessarily satisfies all objectives. However, the majority of points do, and the others are close to the experimental bounds. In general, both NSGA-III and h-CMA-ES demonstrate a tendency to replicate points within the same parameter regions as those identified by the MCMC scan. Additionally, both algorithms discover extra

points beyond the established regions of the MCMC, with h-CMA-ES providing a higher amount and more widely distributed points compared to NSGA-III. Nevertheless, this suggests that while the CI parametrisation in the MCMC scan constrain the parameter space, the smaller region still encompasses a significant portion of the viable parameter space. However, this observation should be approached with caution, considering that the statistical significance of the results obtained by h-CMA-ES is weaker due to the smaller number of points compared to MCMC and NSGA-III.

5.3.1 Couplings

The yukawa couplings g_{F_1}, g_{F_2}, g_Ψ and g_R establish connections between the SM particles and the BSM particles. As such, they play a crucial role in producing neutrino masses, the anomalous magnetic moment of the muon, and influencing processes involving charged lepton flavor violation. This makes them particularly interesting. Each coupling has three components according to the three flavours. Figure 5.2 illustrates the correlations among the absolute values of the components of the g_{F_j} couplings across the three search algorithms. Similarly, Figure 5.3 depicts the correlations associated with the couplings g_Ψ and g_R.

For the results of the MCMC scan, the components of $g_{F_{1,2}}$ exhibit similar behavior, approximately adhering to the upper limit $|g^{\alpha}_{F^i_{1,2}}| \lesssim 10^{-3}$ for $i = 1, 2, 3$. This conformity arises from the imposed constraint on the couplings in (4.20) to simultaneously accommodate neutrino data, Δa_μ, and CLFV processes.

The h-CMA-ES and NSGA-III scans could each replicate portions of the parameter space already discovered by the MCMC. Moreover, these methods identified points beyond these established bounds. Notably, h-CMA-ES demonstrated the ability to locate points with significantly higher values in $g^{1,2}_{F_1}$ and $g^{1,2}_{F_2}$.

The scaling behavior of all components within $g_{F_{1,2}}$ during the MCMC scan is primarily driven by the trilinear coupling α, as illustrated in the left plots of Figure 5.4. This phenomenon arises from the fact that higher values of α correspond to significant scalar mixing, resulting in the suppression of $g_{F_{1,2}}$ due to the neutrino mass fit. While h-CMA-ES successfully replicates this behavior, the NSGA-III results have an insufficient coverage, making it challenging to draw meaningful conclusions.

For g_Ψ, the MCMC scan shows the hierarchy described by (4.20) among its components, which can bee seen in Figure 5.3. As previously mentioned, this hierarchy is designed to accommodate the anomalous magnetic moment of the muon while adhering to the constraints imposed by CLFV processes. Notably, this relationship is associated with the coupling g_R, as both couplings play an equal role in these processes, as illustrated in the diagrams presented in Figure 3.2. To achieve consistency with the observed Δa_μ, both

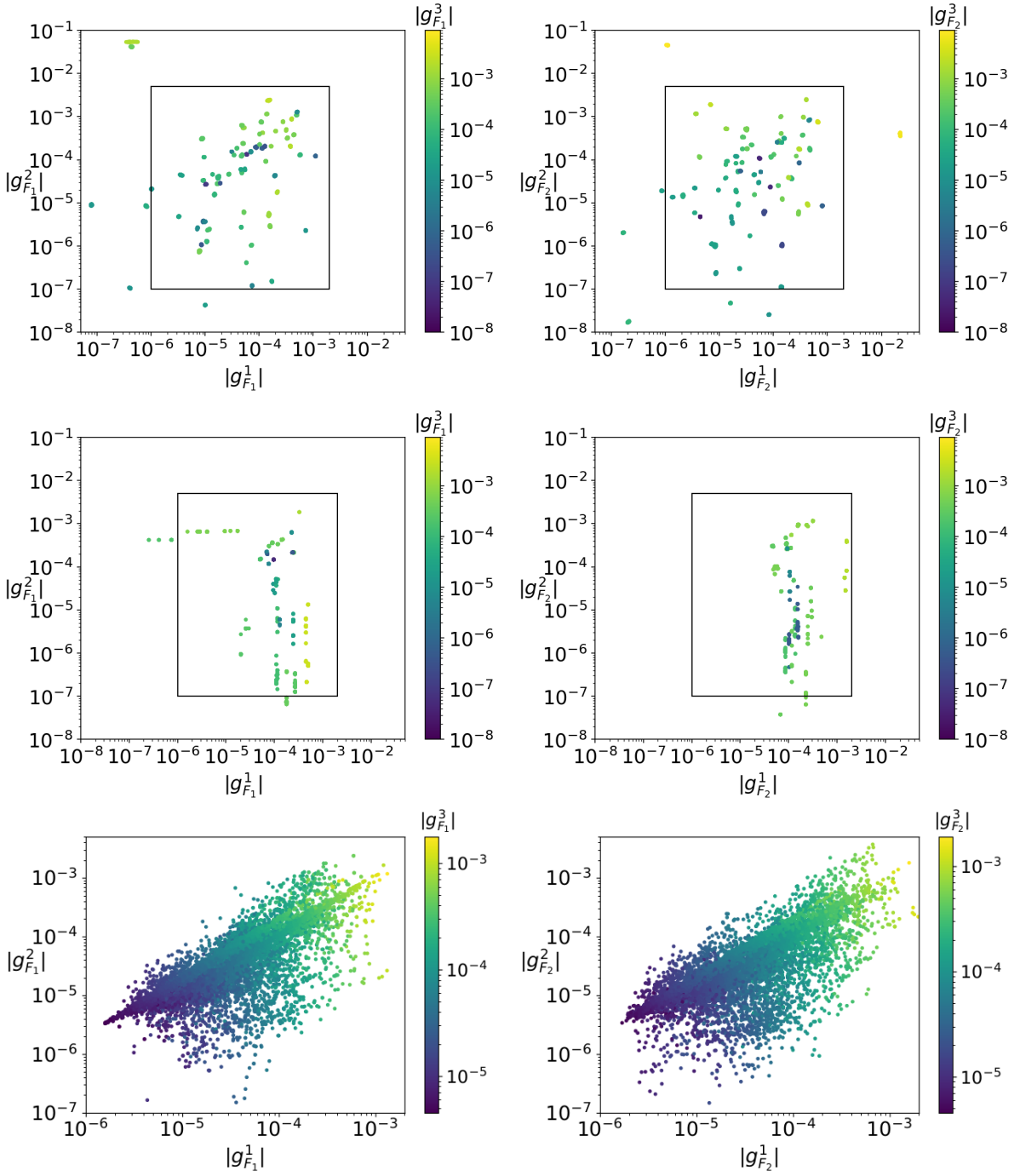

Figure 5.2: Distributions of the absolute values of the components of the Yukawa couplings g_{F_1} (left side) an g_{F_2} (right side), obtained from the three scans h-CMA-ES (upper), NSGA-III (middle) and MCMC [1] (lower). The rectangle depicts the plot range of the MCMC scan. Note that the color map is different for h-CMA-ES, NSGA-III and MCMC.

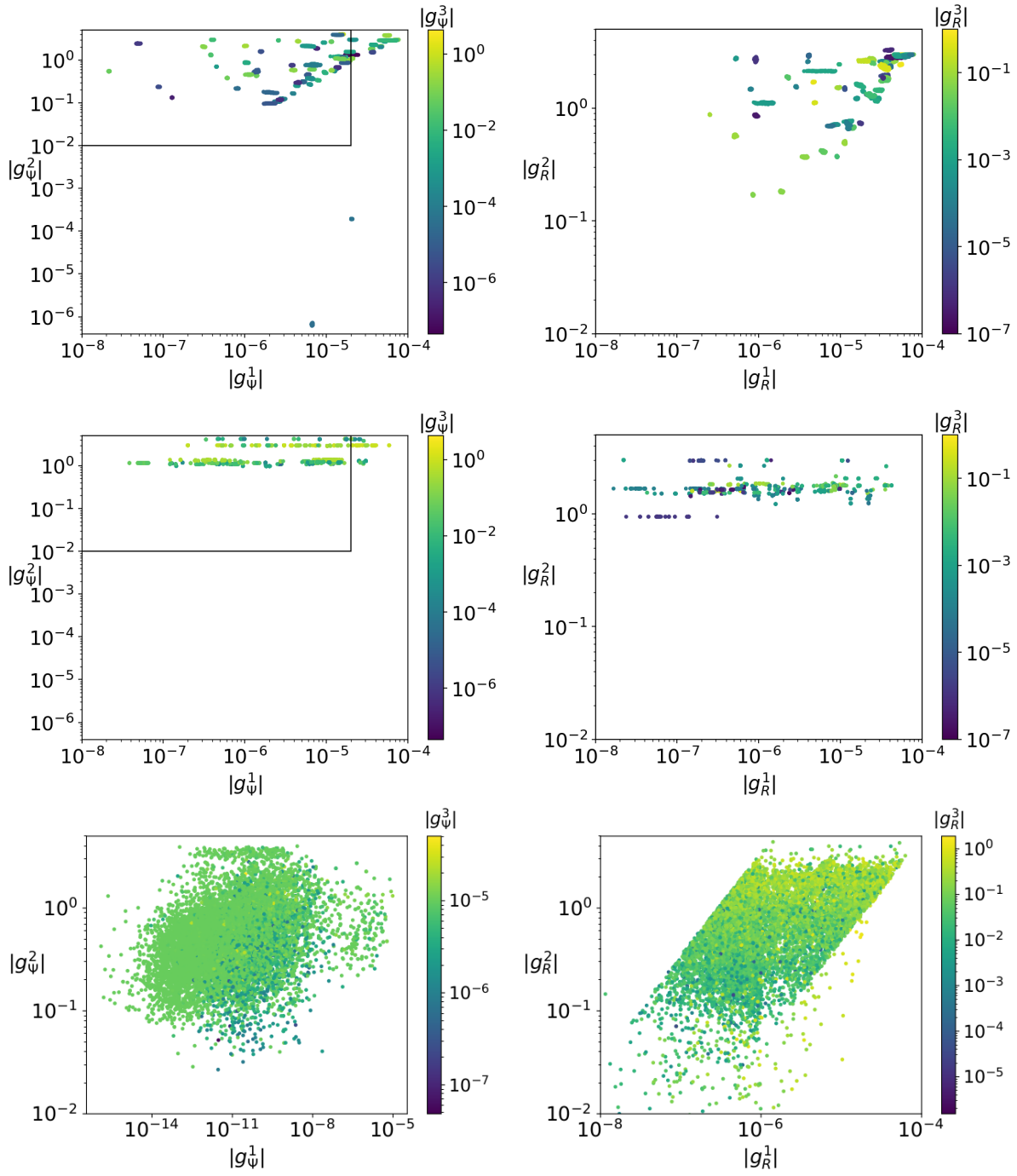

Figure 5.3: Distributions of the absolute values of the components of the Yukawa couplings g_Ψ (left side) and g_R (right side), obtained from the three scans h-CMA-ES (upper), NSGA-III (middle) and MCMC [1] (lower). The rectangle depicts the plot range of the MCMC scan. Note that the color map is different for h-CMA-ES, NSGA-III and MCMC.

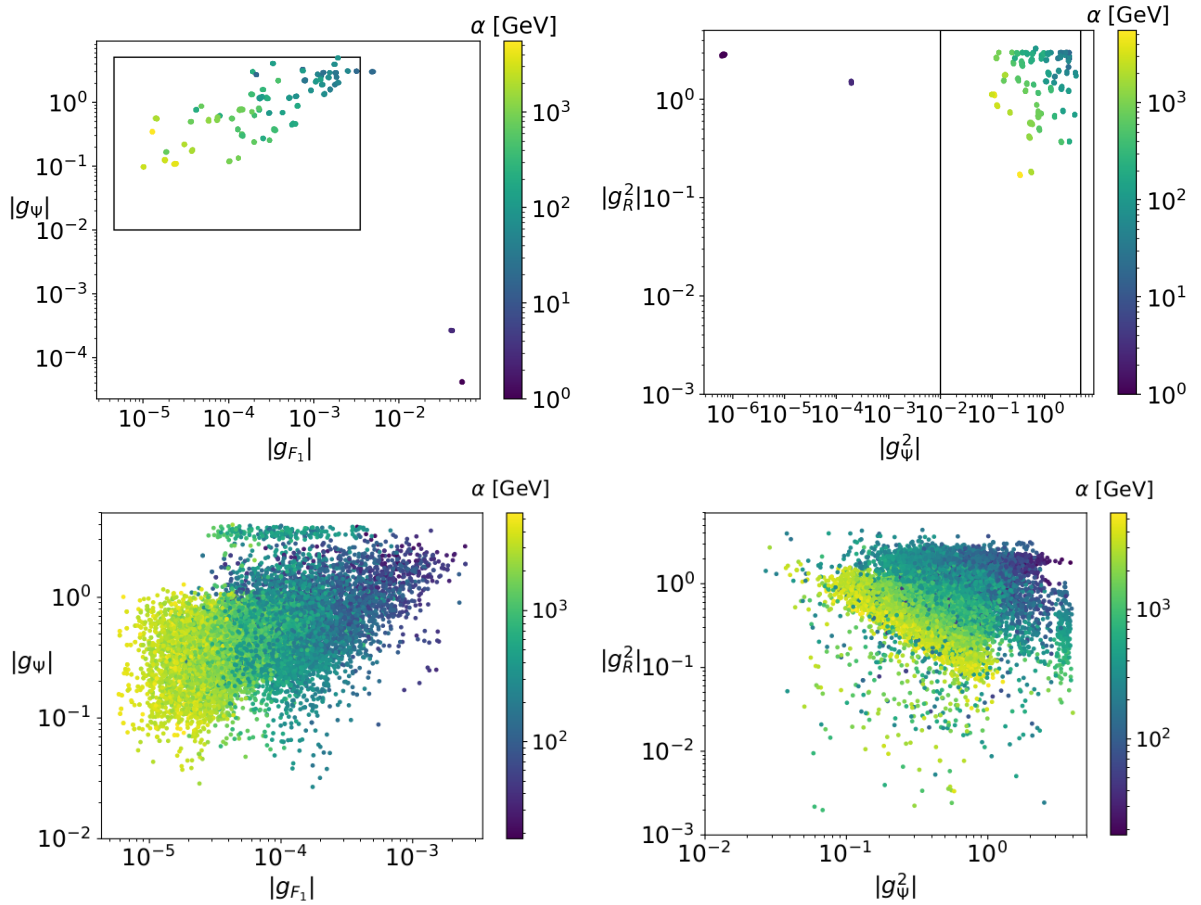

Figure 5.4: Correlations of selected Yukawa couplings with the trilinear coupling α. Obtained from the different scans h-CMA-ES (upper) and MCMC [1] (lower). The rectangle depicts the plot range of the MCMC scan. Note that the color map is different for h-CMA-ES, NSGA-III and MCMC.

couplings g_Ψ^2 and g_R^2 must be sizable. However, a delicate balance is required, necessitating that $g_\Psi^{1,3}$ and $g_R^{1,3}$ remain sufficiently small to avoid surpassing the limits set by $\mathrm{BR}(\mu \to e\gamma)$ and $\mathrm{BR}(\tau \to \mu\gamma)$, respectively. The h-CMA-ES and NSGA-III scans largely mirror the hierarchy observed in $g_{\Psi,R}^1$ and $g_{\Psi,R}^2$. Furthermore, both algorithms identify points beyond the defined limit of $g_\Psi^1 \lesssim 10^{-5}$, with h-CMA-ES revealing instances where $g_\Psi^1 > g_\Psi^2$, deviating from the specified hierarchy. Additionally, both methods identify numerous points featuring increased values in g_Ψ^3, reaching up to approximately 1.

The two clusters with large values in $|g_{F_1}|$ and small values in $|g_\Psi^2|$ represent a completely new parameter region, violating the intuitive hierarchy (4.20) for the couplings and therefore lying outside the parameter ranges of the MCMC scan. They correspond to large values in the Yukawa couplings y_{ij} and therefore facilitating a small mixing in the singlet and doublet fermions.

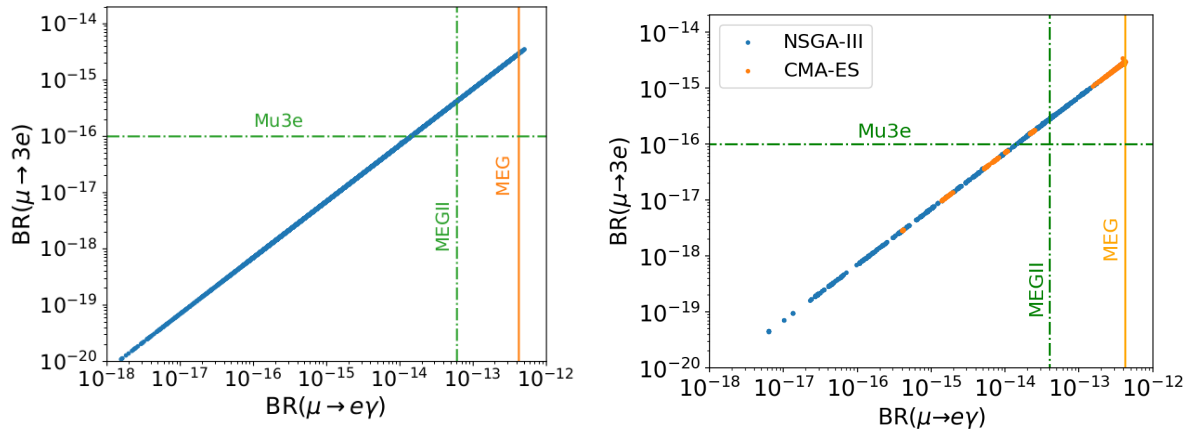

Figure 5.5: Results for the relevant flavor violating muon decays from MCMC [1] (left), h-CMA-ES and NSGA-III (right), with the current limits from the MEG collaboration [46] (full lines) and expected sensitivities (dashed lines) from MEGII [49] and Mu3e [50].

5.3.2 Charged lepton flavour violation

Charged lepton flavor-violating processes play a crucial role in constraining models that propose neutrino mass generation. Essentially, the introduction of non-diagonal Yukawa matrices is necessary to both generate neutrino masses and appropriately fit the mixing angles. This, in turn, establishes a link between charged leptons, enabling transitions between different lepton flavors.

Current limits on the branching ratios for these processes are already strong from the MEG collaboration [46] and Belle [47, 48]. There are plans for experiemnts taking place in the near future like MEGII [49], Mu3e [50] and BelleII [51]. These experiments are anticipated to bring about significant advancements, with an expected sensitivity improvement of up to four orders of magnitude for specific processes, such as $\mu \to 3e$.

In this phenomenological analysis, the outcomes of all three scans align. Consequently, the NSGA-III and h-CMA-ES scans replicate similar results.

The most relevant CLFV decay channels for the muon and the tau are depicted in Figure 5.5 and 5.6 respectively, with the current experimental limits and prospective sensitivities.

Figure 5.5 illustrates a linear relationship between $\mathrm{BR}(\mu \to 3e)$ and $\mathrm{BR}(\mu \to e\gamma)$. This observation indicates that muon decays are predominantly influenced by the dipole contribution, from the penguin diagrams depicted in Figure 3.2.

Tau decays, however, exhibit deviations from linearity, as shown in Figure 5.6. This deviation stems from significant contributions of box diagrams, arising from the elevated values of g_Ψ^2 and g_R^2 needed to fit the anomalous magnetic moment of the muon. Furthermore, with future improvements in sensitivity for these measurements from MEGII, Mu3e and Belle2, a substantial portion of the parameter space can be reached.

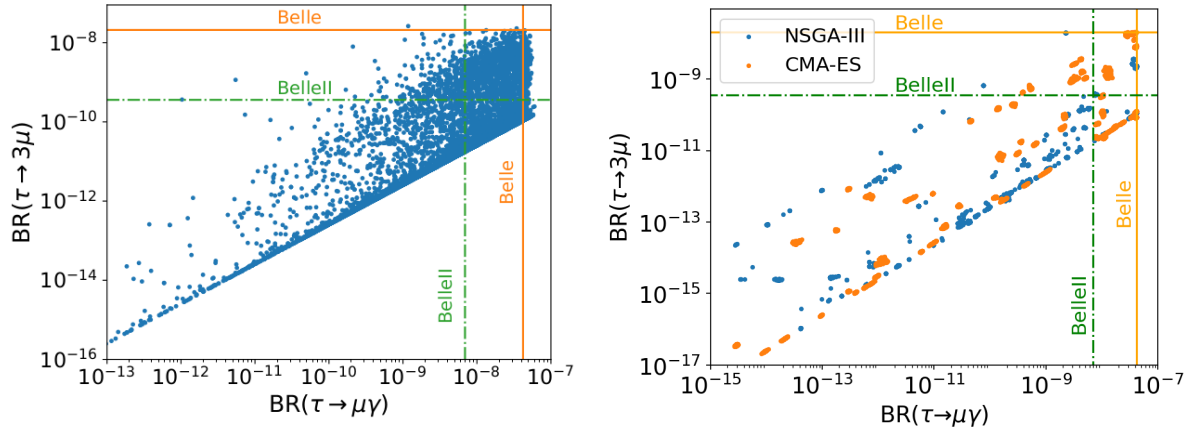

Figure 5.6: Results for the relevant flavor violating tau decays from MCMC [1] (left), h-CMA-ES and NSGA-III (right), with the current limits from Belle [47, 48] (full lines) and expected sensitivities (dashed lines) from Belle II [51].

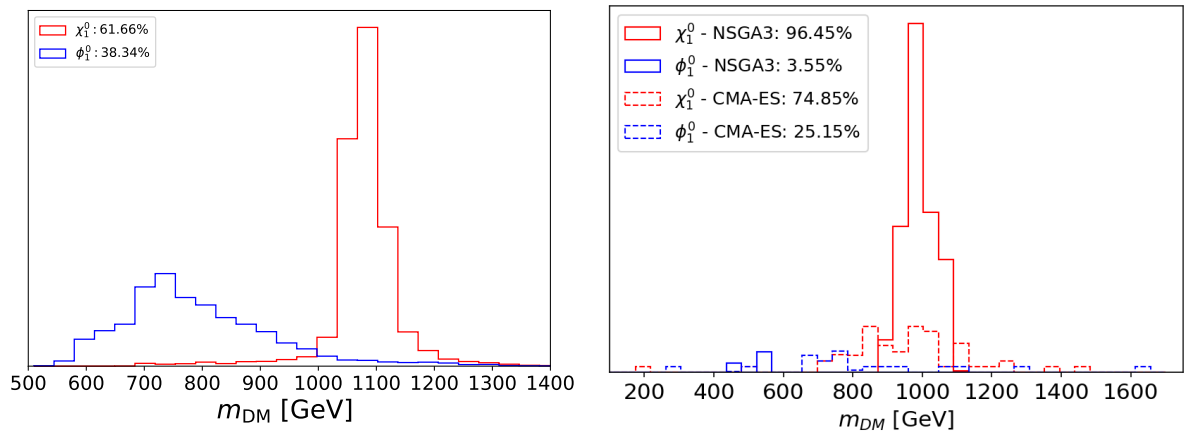

Figure 5.7: Histogram of the mass of the DM candidate, separated into fermionic and scalar DM. Left: MCMC [1]. Right: h-CMA-ES (dashed) and NSGA-III (solid).

For other CLFV processes, the branching ratios remain below 10^{-17}, except in the case of the $\tau \to \mu e^+ e^-$ process, where branching ratios extend up to 10^{-9}, close to the verge of anticipated future sensitivity thresholds.

5.3.3 Dark matter

In the T1-2-A' model there are three candidates for dark matter. These are the lightest fermion χ_1^0, lightest scalar ϕ_1^0 and the pseudo-scalar ϕ_3^0, whichever is lighter in the given parameter configuration. Figure 5.7 displays the distribution of dark matter masses, categorized into fermionic and scalar components. The left side presents results from the MCMC scan [1], while the right side displays outcomes from h-CMA-ES and NSGA-III. In this study the DM candidates are dominated by fermionic particles, about 96% for

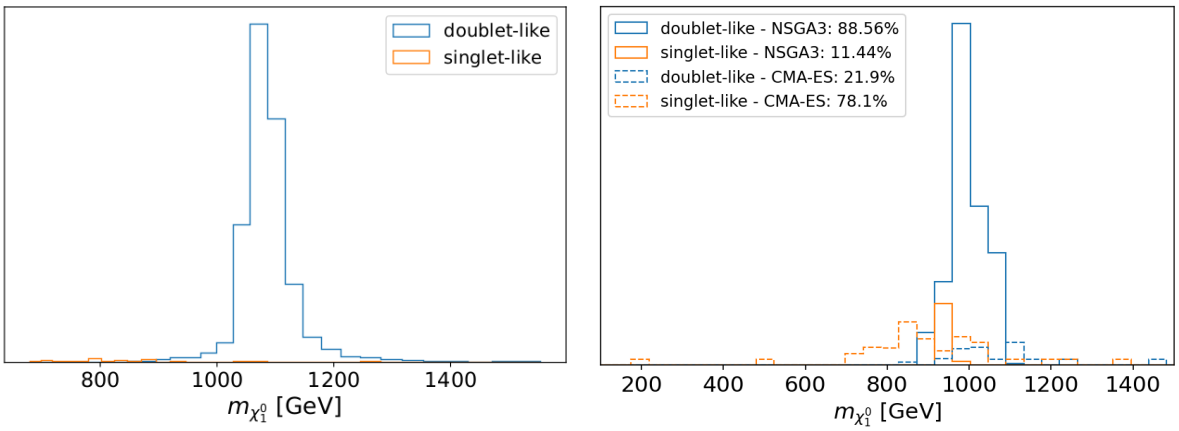

Figure 5.8: Distribution of the mass in case of fermionic DM for the MCMC scan [1] (left), h-CMA-ES and NSGA-III (right), separated into scenarios where the DM candidate is doublet-like (blue) or singlet-like (orange).

NSGA-III and about 75% for h-CMA-ES. The MCMC scan found a greater portion of scalar DM candidates of about 38%. Therefore the amount of valid parameter sets with a scalar DM candidate is insufficient to draw any quantitative conclusions.

As a result, only a partial reproduction of this particular parameter region was achieved, highlighting the necessity for additional data to enhance coverage. Note that for NSGA-III only two runs found scalar DM. This outcome underscores the algorithm's stronger emphasis on specific regions of the parameter space, indicating a limitation in its current formulation.

Pseudo-scalar dark matter has not been identified through any of the applied methodologies. This is attributed to the fact that, within the scalar sector, the mixing among the scalar components is consistently higher, in all three scans, than the mass splitting between the scalar and pseudoscalar. Consequently, the scalar consistently exhibits a lower mass than the pseudoscalar.

The comparison for the fermionic DM case is illustrated in Figure 5.8, distributed into doublet-like and single-like states. It is important to note that the dataset for h-CMA-ES is comparatively small, necessitating a cautious interpretation of these results.

The MCMC scan identified a preferred mass for fermionic DM in the range of 1 TeV to 1.2 TeV. In contrast NSGA-III exhibited a preference for a slightly lower mass range of approximately 0.9 TeV to 1.1 TeV. The h-CMA-ES algorithm demonstrates a significantly broader distribution, encompassing masses ranging from as low as 200 GeV to up to 1.4 TeV. Notably, a preference is observed for masses within the range of 0.7 TeV to 1.1 TeV.

In both the MCMC and NSGA-III scans, the fermionic DM displayed a dominance of doublet-like states, and only minimal mixing of the $SU(2)_L$ singlet and doublet states F_i and Ψ_j. Conversely, the h-CMA-ES scan indicated a prevalence of singlet-like fermionic

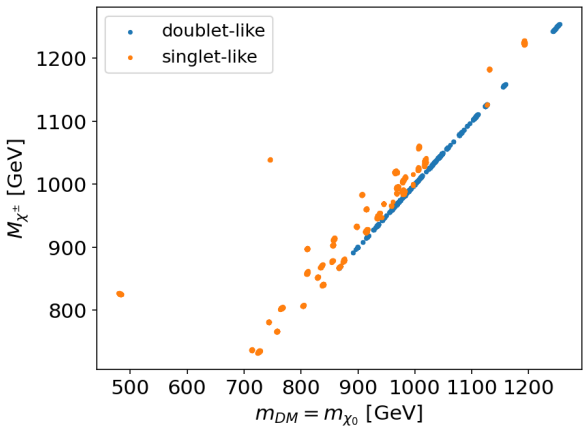

Figure 5.9: Mass of the charged fermion $\chi^{\pm}$ against the DM mass in the case of fermionic DM, differentiated into singlet-like (orange) or doublet-like (blue) DM.

DM and revealed a few points with strong mixing.
For scalar DM the MCMC scan found again a doublet dominated set with a mass preference for 700 GeV. The two converged runs from NSGA-III show singlet-like states with a mass around 500 GeV. For h-CMA-ES the amount of points is relatively low and wide spread between masses of 250 GeV and 1.7 TeV and exhibit a preference for singlet-like DM. While the MCMC scan yielded points with stronger mixing between singlet and doublet, both NSGA-III and h-CMA-ES only exhibit minimal mixing.

5.4 Collider aspects

In this analysis, the valid points of h-CMA-ES and NSGA-III are combined. Note, that in this study SPheno only calculated two body decays. The fermionic doublet like states $\chi^{\pm,0}$ have the same quantum numbers as higgsinos in supersymmetric models. Only decays of $\chi^{\pm,0}$ with a mass lower than 1300 GeV are considered, since the production cross-section $\sigma(pp \to \chi^{\pm}\chi^{0})$ at the LHC, with $\sqrt{s} = 14$ TeV, of these is greater than 0.8 fb [52].
For fermionic DM in scenario the DM particle is doublet-like, the main decay channel is into a pion and a neutral fermion $\chi^{\pm} \to \pi^{\pm}\,\chi_1^0$. With mean lifetimes between $6 \cdot 10^{-12}$ s and $7 \cdot 10^{-10}$ s, this can be visible as displaced vertices. Due to the small mass difference between $\chi^{\pm}$ and χ_1^0 visible in Figure 5.9 the resulting muon from the pion decay would have too low energy for detection. Additionally one point was identified with a primary decay channel into muon and neutral scalar $\chi^{\pm} \to \mu^{\pm}\,\phi_1^0$. Due to the extremely small lifetime of the charged fermion and the small Mass difference between fermion and scalar of 270 MeV the resulting low energy muon would not be detectable.
In the case where the DM particle is singlet-like, there are mass splittings between 200 MeV and 50 GeV. Because only two body decays where calculated, only a few points

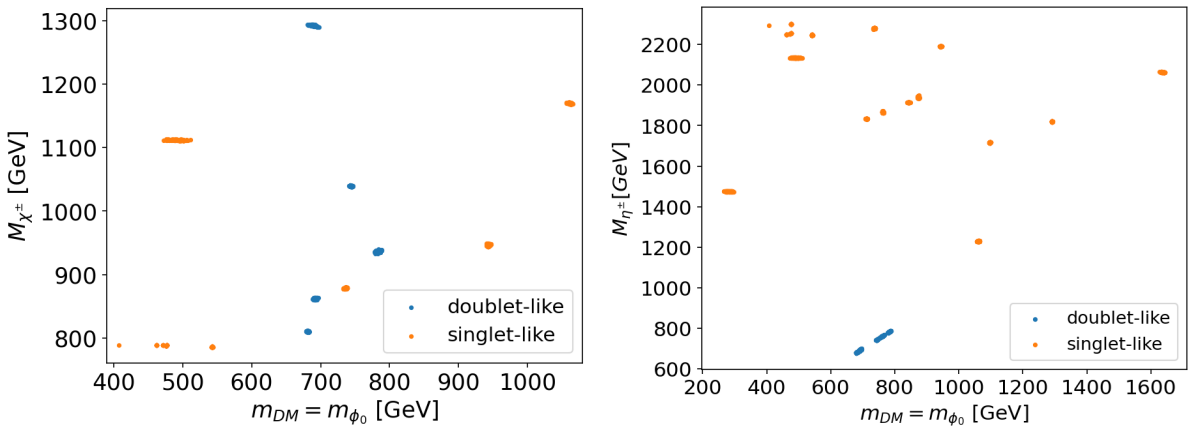

Figure 5.10: Mass of the charged fermion $\chi^\pm$ (left) and charged scalar $\eta^\pm$ (right) against the scalar DM mass, differentiated into singlet-like (orange) or doublet-like (blue) DM.

provide decays of $\chi^\pm$. These had dominant decays into $\chi_1^0 W^\pm$ and $\phi_i^0 \mu^\pm$, with mass differences between 50 GeV and 300 GeV for the charged and neutral BSM particles. As in the MCMC scan additional decay channels would include three final states of which a dominant channel would be $\chi^\pm \to l^\pm \nu \chi_1^0$, with a muon in the final state due to the high Yukawa couplings to the muon.
In the case of scalar DM, the main decay channels are

$$\chi^\pm \to \phi_i^0 \, l_{\mu,\tau}^\pm \,, \tag{5.1}$$

$$\chi_j^0 \to \phi_1^0 \, \nu \,, \; \eta^\mp \, l_{\mu,\tau}^\pm \,, \tag{5.2}$$

where j corresponds to the mass eigenstates that are dominantly $SU(2)_L$ doublets. Due to a small mass splitting of doublet-like fermions χ_j^0, they form a pseudo Dirac doublet. Note, that the mass difference between the charged fermion $\chi^\pm$ and the neutral doublet-like fermions χ_j^0 is smaller than 5 GeV.
The requirement to accommodate Δa_μ results in large couplings to the muon, which is therefore the dominant final state. Due to the high mass difference between 125 GeV and 640 GeV of the fermions and scalars, as can be seen in Figure 5.10 (left), the LHC signal will consist of high energy muons with missing transverse energy. Note, that the mass difference between the charged fermion $\chi^\pm$ and the neutral doublet-like fermions χ_j^0 is smaller than 5 GeV.
For completeness the direct production of the scalar doublet is also possible. But for a mass of 1000 GeV the cross-section is about 0.013 fb, which can be inferred form [52], as they have the same quantum numbers as left-sleptons. From 5.10 one can see, that $m_{\eta^\pm} > 1200$ GeV for a sizeable mass splitting in the scalar sector. Therefore, there will be almost no contribution to the LHC signal from direct production.

Chapter 6

Summary and Outlook

In this thesis the evolutionary algorithms NSGA-III and CMA-ES were introduced and utilized to search the parameter space of the T1-2-A' Scotogenic model. The T1-2-A' Scotogenic model proposed in [1] can explain neutrino masses, the anomalous magnetic moment of the muon, CLFV processes and has a stable DM candidate.
Firstly, the foundational aspects of neutrino masses, the anomalous magnetic moment of the muon, and dark matter were introduced. Subsequently, the T1-2-A' Scotogenic model was presented. In this model the scalar sector is extended by a $SU(2)_L$ singlet S and a doublet η. In the fermion sector two $SU(2)_L$ singlets $F_{1,2}$ and two Weyl fermion doublets $\Psi_{1,2}$ are added. These are all odd under the new $\mathbb{Z}_2$ symmetry while SM particles are even.
Furthermore the evolutionary algorithms NSGA-III and CMA-ES were introduced and the specific implementation of the parameter search for this model was discussed.
A previous investigation of the model by Alvarez et al. [1] presented an analysis of the parameter space using MCMC. In their research, the Casas-Ibarra parmetrisation was used and modified to accommodate neutrino oscillation data and the anomalous magnetic moment of the muon. The results of their work is compared with the results of the new methods in this thesis.
A modification to CMA-ES, termed h-CMA-ES, is proposed which introduces a hierarchy to the objectives and thereby greatly improving the convergence rate. The h-CMA-ES algorithm yields parameter sets that exhibit a more comprehensive coverage of the parameter space. In contrast to NSGA-III, which tends to generate parameter sets in a smaller sub region. But compared to the MCMC scan both NSGA-III and h-CMA-ES provide worse coverage for the shared region of the parameter space. Notably, h-CMA-ES demonstrates a 46% higher sampling efficiency compared to NSGA-III.
Both NSGA-III and h-CMA-ES can reproduce parts of the parameter regions produced in the previous MCMC scan. Additionally new regions outside the previous scope could be identified. Especially h-CMA-ES was able to find two clusters with significantly different

parameter sets.
Due to the significant couplings to the muon, a considerable portion of the parameter space, characterized by elevated branching ratios for the decays $\mu \to e\gamma$, $\mu \to 3e$, $\tau \to \mu\gamma$ and $\tau \to 3\mu$, falls within the potential reach of forthcoming experiments.
Both NSGA-III and h-CMA-ES found a preference for a fermionic DM candidate, comparable to the MCMC scan. NSGA-III found dominantly doublet-like DM with a preferred mass range of 0.9 Tev to 1.1 TeV, which is a bit lighter than the range of 1 TeV to 1.2 TeV found in the MCMC scan. h-CMA-ES displayed a preference for singlet-like DM with a wide spread ranging from 200 GeV to 1.4 TeV.
For the small amount of parameter sets with a scalar DM, h-CMA-ES presented DM candidates with masses ranging from 250 Gev to 1.7 TeV.
Lastly, a brief analysis of LHC phenomenology was conducted, revealing that in the scalar dark matter (DM) case, high-energy muons with missing transverse energy serve as the dominant signal at the LHC.
In the future additional results of both algorithms could improve the current coverage issue. Likewise further modifications to the proposed algorithms can increase the convergence rate and coverage of the parameter space. One proposed improvement concentrates on the introduced hierarchy concept for observables. Including more hierarchy steps according to the difficulty of fitting these observables, could improve the convergence rate further. Another method could combine h-CMA-ES and MCMC by first searching points with h-CMA-ES and subsequently using them as start points for an MCMC scan to improve the sampling efficiency.

References

[1] A. Alvarez et al. "Accommodating muon (g − 2) and leptogenesis in a scotogenic model". In: *JHEP* 06 (2023), p. 163. DOI: 10.1007/JHEP06(2023)163. arXiv: 2301.08485 [hep-ph].

[2] *Tevatron*. https://www.fnal.gov/pub/tevatron/experiments/index.html. accessed 14.01.2024.

[3] Thomas Taylor and Daniel Treille. "The Large Electron Positron Collider (LEP): Probing the Standard Model". In: *Adv. Ser. Direct. High Energy Phys.* 27 (2017). Ed. by Christian Fabjan et al., pp. 217–261. DOI: 10.1142/9789814749145_0007.

[4] O. Gonzalez. "LHC Results Highlights (CLASHEP 2013)". In: *7th CERN–Latin-American School of High-Energy Physics*. 2015, pp. 191–233. DOI: 10.5170/CERN-2015-001.191. arXiv: 1307.6992 [hep-ex].

[5] John N. Bahcall and Raymond Davis. "Solar Neutrinos: A Scientific Puzzle". In: *Science* 191.4224 (1976), pp. 264–267. DOI: 10.1126/science.191.4224.264. eprint: https://www.science.org/doi/pdf/10.1126/science.191.4224.264. URL: https://www.science.org/doi/abs/10.1126/science.191.4224.264.

[6] Christopher W. Walter. "The Super-Kamiokande Experiment". In: (Feb. 2008), pp. 19–43. DOI: 10.1142/9789812771971_0002. arXiv: 0802.1041 [hep-ex].

[7] B. et al. Abi. "Measurement of the Positive Muon Anomalous Magnetic Moment to 0.46 ppm". In: *Phys. Rev. Lett.* 126 (14 Apr. 2021), p. 141801. DOI: 10.1103/PhysRevLett.126.141801. URL: https://link.aps.org/doi/10.1103/PhysRevLett.126.141801.

[8] D. P. et al. Aguillard. "Measurement of the Positive Muon Anomalous Magnetic Moment to 0.20 ppm". In: *Phys. Rev. Lett.* 131 (16 Oct. 2023), p. 161802. DOI: 10.1103/PhysRevLett.131.161802. URL: https://link.aps.org/doi/10.1103/PhysRevLett.131.161802.

[9] F. Zwicky. "Die Rotverschiebung von extragalaktischen Nebeln". In: *Helv. Phys. Acta* 6 (1933), pp. 110–127. DOI: 10.1007/s10714-008-0707-4.

[10] Gianfranco Bertone and Dan Hooper. "History of dark matter". In: *Rev. Mod. Phys.* 90 (4 Oct. 2018), p. 045002. DOI: 10.1103/RevModPhys.90.045002. URL: https://link.aps.org/doi/10.1103/RevModPhys.90.045002.

[11] Cosimo Bambi and Alexandre D. Dolgov. *Introduction to Particle Cosmology: The Standard Model of Cosmology and its Open Problems*. Berlin, Heidelberg: Springer Berlin Heidelberg, 2016. ISBN: 978-3-662-48078-6. DOI: 10.1007/978-3-662-48078-6_1. URL: https://doi.org/10.1007/978-3-662-48078-6_1.

[12] Ernest Ma. "Verifiable radiative seesaw mechanism of neutrino mass and dark matter". In: *Phys. Rev. D* 73 (2006), p. 077301. DOI: 10.1103/PhysRevD.73.077301. arXiv: hep-ph/0601225.

[13] Diego Restrepo, Oscar Zapata, and Carlos E. Yaguna. "Models with radiative neutrino masses and viable dark matter candidates". In: *JHEP* 11 (2013), p. 011. DOI: 10.1007/JHEP11(2013)011. arXiv: 1308.3655 [hep-ph].

[14] Kalyanmoy Deb and Himanshu Jain. "An Evolutionary Many-Objective Optimization Algorithm Using Reference-Point-Based Nondominated Sorting Approach, Part I: Solving Problems With Box Constraints". In: *IEEE Transactions on Evolutionary Computation* 18.4 (2014), pp. 577–601. DOI: 10.1109/TEVC.2013.2281535.

[15] Nikolaus Hansen. "The CMA evolution strategy: a comparing review". In: *Towards a new evolutionary computation: Advances in the estimation of distribution algorithms* (2006), pp. 75–102.

[16] J. A. Casas and A. Ibarra. "Oscillating neutrinos and $\mu \to e, \gamma$". In: *Nucl. Phys. B* 618 (2001), pp. 171–204. DOI: 10.1016/S0550-3213(01)00475-8. arXiv: hep-ph/0103065.

[17] Wolfgang Pauli. "Pauli letter of the 4th of December 1930". Pauli Archive at CERN. URL: https://cds.cern.ch/record/83282.

[18] Clyde L Cowan Jr et al. "Detection of the free neutrino: a confirmation". In: *Science* 124.3212 (1956), pp. 103–104.

[19] Werner Porod. Lecture manuscript, *Theoretical (Elementary) Particle Physics*. Nov. 2020.

[20] Ivan Esteban et al. "The fate of hints: updated global analysis of three-flavor neutrino oscillations". In: *JHEP* 09 (2020), p. 178. DOI: 10.1007/JHEP09(2020)178. arXiv: 2007.14792 [hep-ph].

[21] M. Aker et al. "Direct neutrino-mass measurement with sub-electronvolt sensitivity". In: *Nature Phys.* 18.2 (2022), pp. 160–166. DOI: 10.1038/s41567-021-01463-1. arXiv: 2105.08533 [hep-ex].

[22] X. Fan et al. "Measurement of the Electron Magnetic Moment". In: *Phys. Rev. Lett.* 130 (7 Feb. 2023), p. 071801. DOI: 10.1103/PhysRevLett.130.071801. URL: https://link.aps.org/doi/10.1103/PhysRevLett.130.071801.

[23] Tatsumi Aoyama et al. "Erratum: Tenth-order electron anomalous magnetic moment: Contribution of diagrams without closed lepton loops [Phys. Rev. D 91, 033006 (2015)]". In: *Phys. Rev. D* 96 (1 July 2017), p. 019901. DOI: 10.1103/PhysRevD.96.019901. URL: https://link.aps.org/doi/10.1103/PhysRevD.96.019901.

[24] T. Aoyama et al. "The anomalous magnetic moment of the muon in the Standard Model". In: *Physics Reports* 887 (2020). The anomalous magnetic moment of the muon in the Standard Model, pp. 1–166. ISSN: 0370-1573. DOI: https://doi.org/10.1016/j.physrep.2020.07.006. URL: https://www.sciencedirect.com/science/article/pii/S0370157320302556.

[25] Particle Data Group and R L et al. Workman. "Review of Particle Physics". In: *Progress of Theoretical and Experimental Physics* 2022.8 (Aug. 2022), p. 083C01. ISSN: 2050-3911. DOI: 10.1093/ptep/ptac097. eprint: https://academic.oup.com/ptep/article-pdf/2022/8/083C01/49175539/ptac097.pdf. URL: https://doi.org/10.1093/ptep/ptac097.

[26] Simeon Bird et al. "Snowmass2021 Cosmic Frontier White Paper: Primordial black hole dark matter". In: *Physics of the Dark Universe* 41 (2023), p. 101231. ISSN: 2212-6864. DOI: https://doi.org/10.1016/j.dark.2023.101231. URL: https://www.sciencedirect.com/science/article/pii/S2212686423000651.

[27] Bernard Carr and Florian Kühnel. "Primordial Black Holes as Dark Matter: Recent Developments". In: *Annual Review of Nuclear and Particle Science* 70.1 (2020), pp. 355–394. DOI: 10.1146/annurev-nucl-050520-125911. eprint: https://doi.org/10.1146/annurev-nucl-050520-125911. URL: https://doi.org/10.1146/annurev-nucl-050520-125911.

[28] R. D. Peccei and Helen R. Quinn. "CP Conservation in the Presence of Pseudoparticles". In: *Phys. Rev. Lett.* 38 (25 June 1977), pp. 1440–1443. DOI: 10.1103/PhysRevLett.38.1440. URL: https://link.aps.org/doi/10.1103/PhysRevLett.38.1440.

[29] Thomas Mannel. "Theory and Phenomenology of CP Violation". In: *Nuclear Physics B - Proceedings Supplements* 167 (2007). Proceedings of the 7th International Conference on Hyperons, Charm and Beauty Hadrons, pp. 170–174. ISSN: 0920-5632. DOI: https://doi.org/10.1016/j.nuclphysbps.2006.12.083. URL: https://www.sciencedirect.com/science/article/pii/S0920563206010711.

[30] Nabila Aghanim et al. “Planck 2018 results-VI. Cosmological parameters”. In: *Astronomy & Astrophysics* 641 (2020), A6.

[31] Andreas Crivellin, Martin Hoferichter, and Philipp Schmidt-Wellenburg. “Combined explanations of $(g-2)_{\mu,e}$ and implications for a large muon EDM”. In: *Phys. Rev. D* 98 (11 Dec. 2018), p. 113002. DOI: 10.1103/PhysRevD.98.113002. URL: https://link.aps.org/doi/10.1103/PhysRevD.98.113002.

[32] Ernesto Arganda and Maria J. Herrero. “Testing supersymmetry with lepton flavor violating tau and mu decays”. In: *Phys. Rev. D* 73 (2006), p. 055003. DOI: 10.1103/PhysRevD.73.055003. arXiv: hep-ph/0510405.

[33] Kalyanmoy Deb, Ram Bhushan Agrawal, et al. “Simulated binary crossover for continuous search space”. In: *Complex systems* 9.2 (1995), pp. 115–148.

[34] Eyal Wirsansky. *Hands-on genetic algorithms with Python: applying genetic algorithms to solve real-world deep learning and artificial intelligence problems*. Packt Publishing Ltd, 2020.

[35] Kalyanmoy Deb and Debayan Deb. “Analysing mutation schemes for real-parameter genetic algorithms”. In: *International Journal of Artificial Intelligence and Soft Computing* 4.1 (2014), pp. 1–28.

[36] Nikolaus Hansen. *The CMA Evolution Strategy: A Tutorial*. 2023. arXiv: 1604.00772 [cs.LG].

[37] K. Deb et al. “A fast and elitist multiobjective genetic algorithm: NSGA-II”. In: *IEEE Transactions on Evolutionary Computation* 6.2 (2002), pp. 182–197. DOI: 10.1109/4235.996017.

[38] *Distributed Evolutionary Algorithms in Python DEAP*. GitHub repository. URL: https://github.com/deap/deap.

[39] Florian Staub. “SARAH 4 : A tool for (not only SUSY) model builders”. In: *Comput. Phys. Commun.* 185 (2014), pp. 1773–1790. DOI: 10.1016/j.cpc.2014.02.018. arXiv: 1309.7223 [hep-ph].

[40] W. Porod and F. Staub. “SPheno 3.1: Extensions including flavour, CP-phases and models beyond the MSSM”. In: *Comput. Phys. Commun.* 183 (2012), pp. 2458–2469. DOI: 10.1016/j.cpc.2012.05.021. arXiv: 1104.1573 [hep-ph].

[41] Werner Porod, Florian Staub, and Avelino Vicente. “A Flavor Kit for BSM models”. In: *Eur. Phys. J. C* 74.8 (2014), p. 2992. DOI: 10.1140/epjc/s10052-014-2992-2. arXiv: 1405.1434 [hep-ph].

[42] Geneviève Bélanger et al. "micrOMEGAs5.0 : Freeze-in". In: *Comput. Phys. Commun.* 231 (2018), pp. 173–186. DOI: 10.1016/j.cpc.2018.04.027. arXiv: 1801.03509 [hep-ph].

[43] Andreas Karle. *Parameter space exploration with evolutionary algorithms*. GitLab repository. URL: https://gitlab.com/lip_ml/parameter_scan.

[44] Christian Igel, Nikolaus Hansen, and Stefan Roth. "Covariance Matrix Adaptation for Multi-objective Optimization". In: *Evolutionary computation* 15 (Feb. 2007), pp. 1–28. DOI: 10.1162/evco.2007.15.1.1.

[45] Takuya Akiba et al. "Optuna: A Next-generation Hyperparameter Optimization Framework". In: *Proceedings of the 25th ACM SIGKDD International Conference on Knowledge Discovery and Data Mining*. 2019.

[46] A. M. Baldini et al. "Search for the lepton flavour violating decay $\mu^+ \to e^+\gamma$ with the full dataset of the MEG experiment". In: *Eur. Phys. J. C* 76.8 (2016), p. 434. DOI: 10.1140/epjc/s10052-016-4271-x. arXiv: 1605.05081 [hep-ex].

[47] A. Abdesselam et al. "Search for lepton-flavor-violating tau-lepton decays to $\ell\gamma$ at Belle". In: *JHEP* 10 (2021), p. 19. DOI: 10.1007/JHEP10(2021)019. arXiv: 2103.12994 [hep-ex].

[48] K. Hayasaka et al. "Search for Lepton Flavor Violating Tau Decays into Three Leptons with 719 Million Produced Tau+Tau- Pairs". In: *Phys. Lett. B* 687 (2010), pp. 139–143. DOI: 10.1016/j.physletb.2010.03.037. arXiv: 1001.3221 [hep-ex].

[49] Manuel Meucci. "MEG II experiment status and prospect". In: *PoS* NuFact2021 (2022), p. 120. DOI: 10.22323/1.402.0120. arXiv: 2201.08200 [hep-ex].

[50] A. Blondel et al. "Research Proposal for an Experiment to Search for the Decay $\mu \to eee$". In: (Jan. 2013). arXiv: 1301.6113 [physics.ins-det].

[51] Swagato Banerjee. "Searches for Lepton Flavor Violation in Tau Decays at Belle II". In: *Universe* 8.9 (2022), p. 480. DOI: 10.3390/universe8090480. arXiv: 2209.11639 [hep-ex].

[52] *LHC SUSY Cross Section Working Group*. https://twiki.cern.ch/twiki/bin/view/LHCPhysics/SUSYCrossSections. Accessed: 2024-01-12.

Appendix

A Neutrino mass diagrams

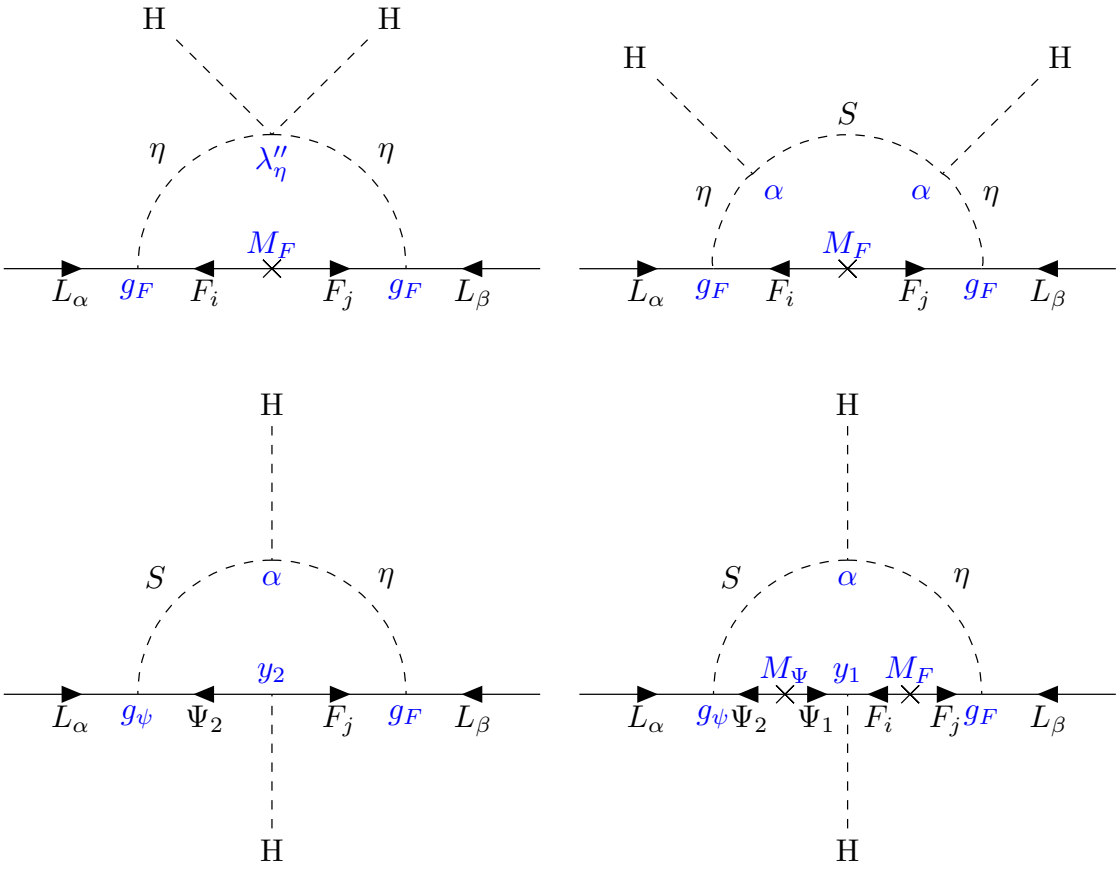

Figure A.1: Diagrams for neutrino mass generation in gauge basis. The vertex factors are depicted in blue. The arrows indicate the flow of hypercharge. The top two diagrams are $\sim g_F^2$. The middle two diagrams are $\sim g_F g_\Psi$.

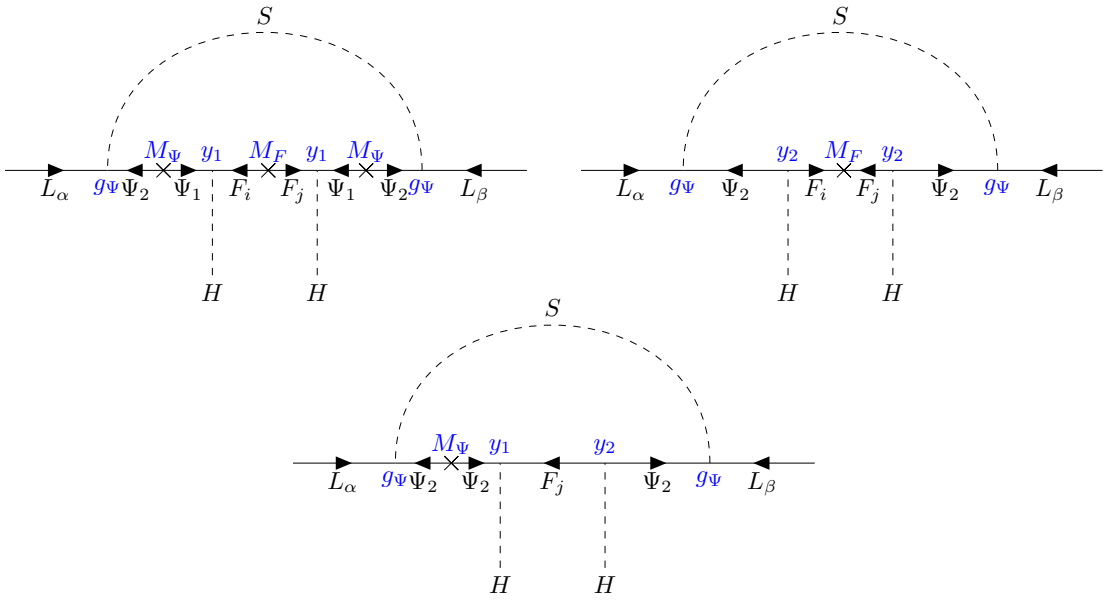

Figure A.2: Diagrams $\sim g_\Psi^2$ for neutrino mass generation in gauge basis. The vertex factors are depicted in blue. The arrows indicate the flow of hypercharge.

B CLFV loop functions

Loop functions for the calculation of the Wilson coefficients in equation (3.30)

$$
\begin{aligned}
f(x) &= \frac{x^2 - 1 - 2x\log(x)}{4(x-1)^3}\,, \\
g(x) &= \frac{x - 1 - \log(x)}{2(x-1)^2}\,, \\
\tilde{f}(x) &= \frac{2x^3 + 3x^2 - 6x + 1 - 6x^2\log(x)}{24(x-1)^4}\,, \\
\tilde{g}(x) &= \frac{1}{2} f(x)\,.
\end{aligned}
\tag{B.1}
$$

C Crossover and mutation operations in NSGA-III

Simulated binary crossover

For the mating or crossover the simulated binary crossover (SBX) bounded is used. This explenation is based on [34]. The SBX takes two parent individuals and creates two offspring individuals.

$$\begin{aligned} offspring_1 &= \frac{1}{2}\left[(1+\beta)parent_1 + (1-\beta)parent_2\right] , \\ offspring_2 &= \frac{1}{2}\left[(1-\beta)parent_1 + (1+\beta)parent_2\right] , \end{aligned} \tag{C.1}$$

where β is a real random number. The average of the offspring is the same as the average of the parents. Additionally this formula has the following properties.

- For $\beta = 1$, the offspring is the same as the parents
- For $\beta < 1$, the offspring values are closer to each other then the parents
- for $\beta > 1$, the offspring values are further apart then the parents

The SBX is designed to produce offspring similar to the parents. Therefore the random value β should have a higher probability for values close to 1. Therefore another uniform distributed random value u in the interval $[0, 1]$, is used to calculate β with the following formula

$$\begin{aligned} \beta &= (2u)^{\frac{1}{\eta_c+1}} && \text{for } u \leq 0.5 , \\ \beta &= \left(\frac{1}{2(1-u)}\right)^{\frac{1}{\eta_c+1}} && \text{for } u > 0.5 , \end{aligned} \tag{C.2}$$

with the crowding degree parameter η_c. A higher value of η_c tends to result in offspring closely resembling the parents, while a lower value of η_c leads to greater dissimilarity among the offspring.

Polynomial mutation

For the mutation the polynomial bounded mutation operator is used [35]. As the name suggests, a polynomial distribution is employed to perturb the individual within its vicinity. The probability distribution on both the left and right sides of the variable value is adjusted, ensuring that no values outside the specified range $[a, b]$ are generated by the mutation operator. For a given parent solution $p \in [a, b]$, the mutated individual p' is calculated using a uniform distributed random number u in the interval $[0, 1]$ as follows

$$\begin{aligned} p' &= p + \left((2u)^{\frac{1}{\eta_m+1}} - 1\right)(p-a) && \text{for } u \leq 0.5 , \\ p' &= p + \left(1 - (2-2u)^{\frac{1}{\eta_m+1}}\right)(b-p) && \text{for } u > 0.5 , \end{aligned} \tag{C.3}$$

with the crowding degree parameter η_m. A higher value of η_m tends to produce minor deviations, while a lower value creates more pronounced mutations.

D NSGA-III pseudo code

The following pseudo code for NSGA-III is based on the approach of Kalyanmoy Deb et al. [14]. Algorithm 1 represents one generational update of NSGA-III, which utilizes the procedures in the Algorithms 2, 3 and 4.

Algorithm 1 Generation t of NSGA-III procedure

Input: H reference points Z^r, parent population P_t

Output: P_{t+1}

$S_t = \emptyset, i = 1$

$Q_t =$ Recombination+Mutation(Pt)

$R_t = P_t \cup Q_t$

$(F_1, F_2, \ldots) =$ Non-dominated-sort(R_t)

repeat

  $S_t = S_t \cup F_i$ and $i = i + 1$

until $|S_t| \geq N$

Last front to be included: $F_l = F_i$

if $|S_t| = N$ **then**

  $P_{t+1} = S_t$, break

else

  $P_{t+1} = \bigcup_{j=1}^{l-1} F_j$

  Points to be chosen from F_l: $K = N - |P_{t+1}|$

  Normalize objectives:
  $f^n =$ `Normalize`(S_t)

  Associate each member s of S_t with a reference point:
  $[\pi(s), d(s)] =$ `Associate`(S_t, Z^r) % $\pi(s)$: closest reference point,
  d: distance between s and $\pi(s)$

  Compute niche count of reference point $j \in Z^r$:
  $\rho_j = \sum_{s \in S_t / F_l}$(**if** $\pi(s) = j$; **then** 1; **else** 0)

  Choose K members, one at a time from F_l to construct P_{t+1}:
  `Niching`$(K, \rho_j, \pi, d, Z^r, F_l, P_{t+1})$

end if

Algorithm 2 `Normalize`(S_t) procedure

Input: S_t *(structured points)*

Output: f^n *(reference points on normalized hyper-plane)*

for $j = 1$ to M **do**
    Compute ideal point: $z_j^{\min} = \min_{s \in S_t} f_j(s)$
    Translate objectives: $f_j(s) = f_j(s) - z_j^{\min}$ for all $s \in S_t$
    Compute extreme points $(z_j^{\max}, j = 1, \ldots, M)$ of S_t
end for
Compute intercepts a_j for $j = 1, \ldots, M$
Normalize objectives (f^n)

Algorithm 3 Associate(S_t, Z^r) procedure

Input: Z^r, S_t

Output: $\pi(s \in S_t), d(s \in S_t)$

for each reference point $z \in Z^r$ **do**
    Compute reference line $w = z$
end for
for each $s \in S_t$ **do**
    for each $w \in Z^r$ **do**
        Compute $d_\perp(s, w) = \left\| s - w^T s w / \|w\|^2 \right\|$
    end for
    Assign $\pi(s) = w : \text{argmin}_{w \in Z^r} d^\perp(s, w)$
    Assign $d(s) = d^\perp(s, \pi(s))$
end for

Algorithm 4 `Niching` $(K, \rho_j, \pi, d, Z^r, F_l, P_{t+1})$ procedure

Input: $K, \rho_j, \pi(s \in S_t), d(s \in (S_t), Z^r, F_l, P_{t+1}$

$k = 1$
while $k \leq K$ **do**
    $J_{\min} = \{j : \text{argmin}_{j \in Z^r} \rho_j\}$
    $\hat{j} = \text{random}(J_{\min})$
    $I_{\hat{j}} = \{s : \pi(s) = \hat{j}, s \in F_l\}$
    if $I_{\hat{j}} \neq \emptyset$ **then**
        if $\rho_{\hat{j}} = 0$ **then**
            $P_{t+1} = P_{t+1} \cup \{s : \text{argmin}_{s \in I_{\hat{j}}} d(s)\}$
        else
            $P_{t+1} = P_{t+1} \cup \{\text{random}(I_{\hat{j}})\}$
        end if
        $\rho_{\hat{j}} = \rho_{\hat{j}} + 1$, $F_l = F_l \backslash \{s\}$
        $k = k + 1$
    else
        $Z_r = Z_r / \{\hat{j}\}$
    end if
end while

E λ couplings and scalar mass parameters

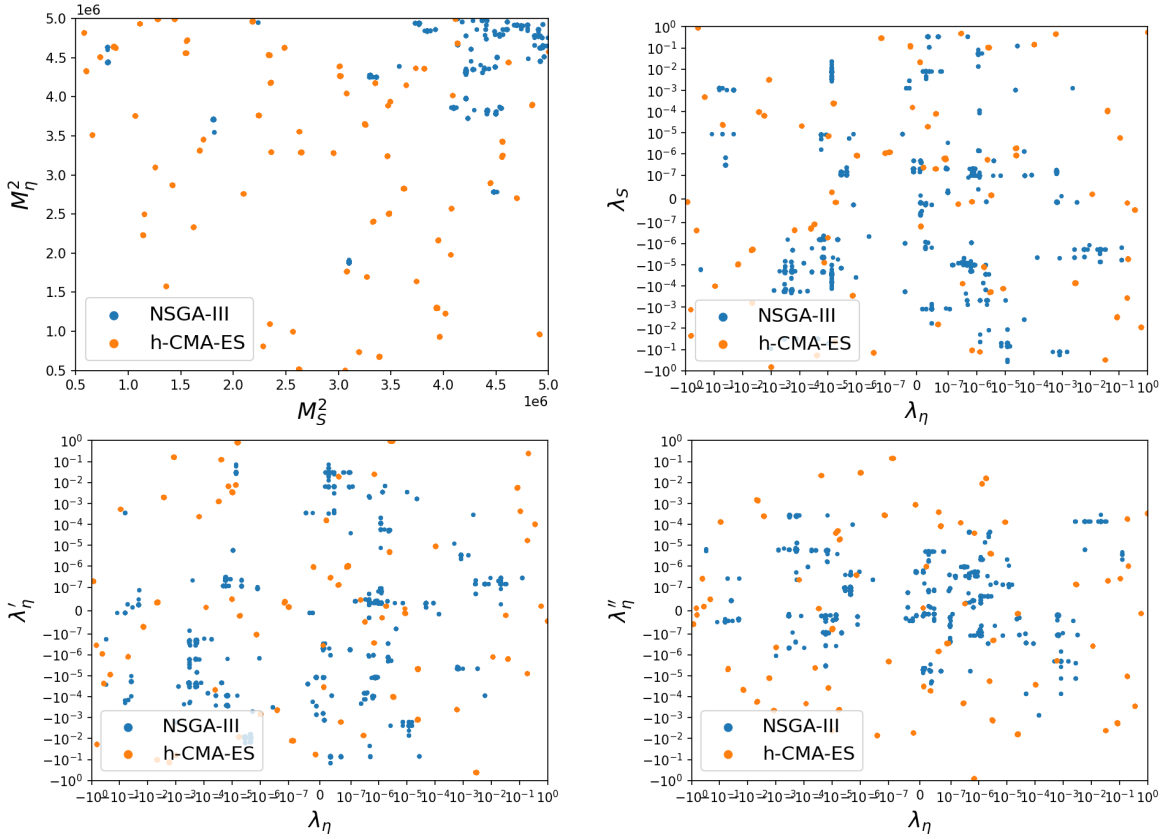

Figure E.1: Scalar mass parameters and a selection of scalar couplings for NSGA-III and h-CMA-ES. h-CMA-ES demonstrates a higher spread and better coverage, compared to NSGA-III, which displays characteristically forming lines and crosses.

Acknowledgements

I want to thank my supervisor, Prof. Dr. Werner Porod for teaching me the foundations of particle physics and the Standard Model, for patience with questions and for guidance during my work on this project.
I am grateful to Miguel Romão for guidance and valuable advice throughout the project. I am also thankful to Fernando Abreu de Souza for mutual support during the whole project.
Finally I want to thank my family and friends for the love and support. I would like to particular thank Bengt Bolsenkötter and Lioba Avenarius for support in stressful times.

Eigenständigkeitserklärung

Hiermit versichere ich, dass ich die vorliegende Masterarbeit selbstständig angefertigt und keine anderen als die in der Arbeit angegebenen Quellen und Hilfsmittel benutzt habe. Sämtliche wörtlichen oder sinngemäßen Übernahmen und Zitate sind kenntlich gemacht und nachgewiesen.
Die Arbeit wurde bisher keiner anderen Prüfungsbehörde zur Erlangung eines akademischen Grades vorgelegt und auch nicht veröffentlicht.

Würzburg, 15. Januar 2024 Andreas Karle .....